Finite Element Modeling of the Behavior of Armor Materials Under High Strain Rates and Large Strains

by

Ioannis Polyzois

A Thesis submitted to the Faculty of Graduate Studies of

The University of Manitoba

in partial fulfillment of the requirements of the degree of

Master of Science

Department of Mechanical and Manufacturing Engineering

University of Manitoba

Winnipeg, Manitoba, Canada

ABSTRACT

For years high strength steels and alloys have been widely used by the military for making armor plates. Advances in technology have led to the development of materials with improved resistance to penetration and deformation. Until recently, the behavior of these materials under high strain rates and large strains has been primarily based on laboratory testing using the Split Hopkinson Pressure Bar apparatus. With the advent of sophisticated computer programs, computer modeling and finite element simulations are being developed to predict the deformation behavior of these metals for a variety of conditions similar to those experienced during combat.

In the present investigation, a modified direct impact Split Hopkinson Pressure Bar apparatus was modeled using the finite element software ABAQUS 6.8 for the purpose of simulating high strain rate compression of specimens of three armor materials: maraging steel 300, high hardness armor (HHA), and aluminum alloy 5083. These armor materials, provided by the Canadian Department of National Defence, were tested at the University of Manitoba by others. In this study, the empirical Johnson-Cook visco-plastic and damage models were used to simulate the deformation behavior obtained experimentally. A series of stress-time plots at various projectile impact momenta were produced and verified by comparison with experimental data. The impact momentum parameter was chosen rather than projectile velocity to normalize the initial conditions for each simulation. Phenomena such as the formation of adiabatic shear bands caused by deformation at high strains and strain rates were investigated through simulations.

It was found that the Johnson-Cook model can accurately simulate the behavior of body-centered cubic (BCC) metals such as steels. The maximum shear stress was calculated for each simulation at various impact momenta. The finite element model showed that shear failure first occurred in the center of the cylindrical specimen and propagated outwards diagonally towards the front and back edges forming an hourglass pattern. This pattern matched the failure behavior of specimens tested experimentally, which also exhibited failure through the formation of adiabatic shear bands. Adiabatic shear bands are known to lead to a complete shear failure. Both mechanical and thermal mechanisms contribute to the formation of shear bands. However, the finite element simulations did not show the effects of temperature rise within the material, a phenomenon which is known to contribute to thermal instabilities, whereby strain hardening effects are outweighed by thermal softening effects and adiabatic shear bands begin to form. In the simulations, the purely mechanical maximum shear stress failure, nucleating from the center of the specimens, was used as an indicator of the time at which these shear bands begin to form. The time and compressive stress at the moment of thermal instability in experimental results which have shown to form adiabatic shear bands, matched closely to those at which shear failure was first observed in the simulations.

Although versatile in modeling BCC behavior, the Johnson-Cook model did not show the correct stress response in face-centered cubic (FCC) metals, such as aluminum 5083, where effects of strain rate and temperature depend on strain. Similar observations have been reported in literature. In the Johnson-Cook model, temperature, strain rate and strain parameters are independent of each other. To this end, a more physical-based

model based on dislocation mechanics, namely the Feng and Bassim constitutive model, would be more appropriate.

ACKNOWLEDGEMENTS

I wish to convey my sincere appreciation to my thesis supervisor, Professor M.N. Bassim, for his continued enthusiasm, valuable guidance, and ongoing support throughout this project.

I would also like to extend my gratitude to the other members of my thesis committee, Professors A. Shalaby and I. Telichev for their valuable input and constructive comments on the draft of this thesis.

Special thanks go to Ghaznafar M. Nazimuddin for introducing me to the field of high strain rate experimentation and providing me with valuable experimental data which were used to verify the theoretical models presented in thesis.

The financial support provided by the Canadian Department of National Defence is gratefully acknowledged.

Finally, I would like to extend my heartfelt thanks to my family, for their unremitting support and encouragement.

TABLE OF CONTENTS

ABSTRACT ..... **II**

ACKNOWLEDGEMENTS ..... **V**

TABLE OF CONTENTS ..... **VI**

LIST OF FIGURES ..... **IX**

LIST OF TABLES ..... **XII**

1. INTRODUCTION **1**

1.1. PROBLEM STATEMENT 1

1.2. RESEARCH OBJECTIVES 3

1.3. RESEARCH METHODOLOGY 4

1.4. SCOPE OF WORK 5

2. REVIEW OF RELATED LITERATURE **7**

2.1. DEFORMATION MECHANISMS IN METALS BASED ON DISLOCATION MECHANICS 7

2.1.1. Plastic Deformation in BCC and FCC Metals: 12

2.2. EMPIRICAL AND PHYSICAL BASED CONSTITUTIVE MODELS FOR DESCRIBING THE DEFORMATION BEHAVIOR OF METALS 15

2.2.1. Physical-based Constitutive Models: 16

2.2.1.1. The Zerilli-Armstrong Physical-based Constitutive Model: 20

2.2.2. The Empirical Johnson-Cook Constitutive Model: 22

2.2.2.1. Johnson-Cook Hardening Law: 22

2.2.2.2. Johnson-Cook Strain Rate Dependence: 23

2.2.2.3. The Johnson-Cook Dynamic Failure Model: 24
2.2.2.4. Damage Initiation and Damage Evolution: 25
2.3. ADIABATIC CONDITION IN METALS SUBJECT TO HIGH STRAIN RATE DEFORMATION AND THE FORMATION OF ADIABATIC SHEAR BANDS: 26
2.4. MECHANICAL AND THERMAL INSTABILITIES DURING HIGH STRAIN RATE DEFORMATION: 29
2.5. CURRENT RESEARCH IN THE FIELD OF MICROSTRUCTURAL FINITE ELEMENT MODELING OF METALS 34
3. HIGH STRAIN RATE EXPERIMENTATION 37
3.1. EXPERIMENTAL WORK CONDUCTED AT THE UNIVERSITY OF MANITOBA 41
4. FINITE ELEMENT MODELING 48
4.1. INTRODUCTION.....48
4.2. DETERMINATION OF THE JOHNSON-COOK PLASTICITY COEFFICIENTS FOR EACH ARMOR MATERIAL.....48
4.2.1. Maraging Steel 300: 48
4.2.1.1. Step 1: Analyzing the Quasi-static Stress Strain curve for Maraging Steel 300 in Compression:..... 50
4.2.1.2. Step 2: Determination of the Strain Rate Sensitivity Parameter 'C': 56
4.2.1.3. Step 3: Determination of the Thermal Softening Coefficient 'm':..... 58
4.2.2. High Hardness Armor: 59
4.2.3. Aluminum Alloy 5083:.....60
4.3. FINITE ELEMENT SOFTWARE PACKAGE ABAQUS 6.8.....64
4.4. IMPLEMENTATION OF MATERIAL PARAMETERS INTO ABAQUS.....64

4.5. MODELING THE MODIFIED SPLIT HOPKINSON BAR APPARATUS IN ABAQUS.....69

4.5.1. Design:.....69

5. RESULTS AND DISCUSSION.....74

5.1. SHEAR FAILURE ANALYSIS 74

5.2. STRESS-TIME RESULTS FOR MARAGING STEEL 300.....80

5.3. STRESS-TIME RESULTS FOR HIGH HARDNESS ARMOR.....86

5.4. STRESS-TIME RESULTS FOR ALUMINUM ALLOY 5083-H131 91

6. CONCLUSIONS.....97

REFERENCES.....99

LIST OF FIGURES

Figure 1. HCP, FCC, and BCC, unit cell structures 7

Figure 2. Slipping of two atomic planes in a simple crystalline structure 8

Figure 3. Types of point defects in a crystalline lattice 9

Figure 4. Positive edge dislocation and left-hand screw dislocation of a simple cubic lattice 10

Figure 5. Burgers vector in a perfect crystal showing the lattice distortion of an edge dislocation(Hull and Bacon 2001) 11

Figure 6. Burgers vector in a perfect crystal showing the lattice distortion of a screw dislocation(Hull and Bacon 2001) 11

Figure 7. True tensile stress-strain curve of a BCC polycrystal and the resolved shear stress-strain curve of a single crystal (Hull and Bacon 2001)..... 14

Figure 8. Optical micrograph showing white etching band and deformed band in the microstructure of AISI 4340 steel after impact (A. Odeshi, M. Bassim, et al. 2005) 28

Figure 9. Method of loading and dynamic considerations for metals deformed at various strain rates (U. Lindholm 1971) 37

Figure 10. Schematic of Split Hopkinson Pressure Bar (The American Society of Mechanical Engineers 2006)..... 39

Figure 11. Torsional Split Hopkinson Pressure Bar Apparatus (Yazdani, Bassim and Odeshi 2009) 40

Figure 12. TSHPB Specimen Schematics (Yazdani, Bassim and Odeshi 2009)..... 40

Figure 13. Direct Impact Split Hopkinson Pressure Bar used at The University of Manitoba (Mirfakhraei 2008)..... 42

Figure 14. Quasi-static stress-strain curves for Maraging Steel 300 at various temperatures (ASM International 2002) 51

Figure 15. Constructed Stress-Strain curve for annealed Maraging Steel 300. 52

Figure 16. Plastic region of the stress-strain curve for annealed maraging steel 300... 53

Figure 17. Log Plastic Stress vs. Log Plastic Strain for maraging steel 300 55

Figure 18. Dynamic to Static Stress Ratio vs. ln(Strain Rate) for Maraging Steel 300 58

Figure 19. Quasi-static Tensile Stress Strain Curve for Aluminum Alloy 5083-O 62

Figure 20. Johnson-Cook Approximation to the Plastic QS Stress-Strain Curve for AA5083-O..... 63

Figure 21. Schematics of modeled apparatus in ABAQUS..... 70

Figure 22. Isometric view of meshed specimen..... 71

Figure 23. Maximum shear stress as a function of time for maraging steel 300 76

Figure 24. Isometric cross section of test specimen 76

Figure 25. Nucleation and propagation of shear failure as a function of distance from the edge (given in % of the total length of the specimen)..... 76

Figure 26. Schematic representation of a 3D view of the adiabatic shear bands formed in cylindrical steel specimens (A. Odeshi, M. Bassim, et al. 2005)..... 77

Figure 27. Cross-sectional shear failure of a maraging steel 300 specimen subject to an impact momentum of 38 kg.m/s 78

Figure 28. Cross-section of Ti-15Mo-5Zr-3Al specimen deformed at 8×10^{-3} /s (Lee, Lin, et al. 2008) 78

Figure 29. Photomicrograph of a longitudinal section of an impacted specimen of AISI 4340 Steel (A. Odeshi, M. Bassim, et al. 2005) 79

Figure 30. Stress-time history of MS300 at an impact momentum of 30.85 kg.m/s 81

Figure 31. Stress-time history of MS300 at an impact momentum of 40.12 kg.m/s 82

Figure 32. Stress-time history of MS300 at an impact momentum of 44.82 kg.m/s 83

Figure 33. Stress-time history of high hardness armor at an impact momentum of 30.85 kg.m/s 87

Figure 34. Stress-time history of high hardness armor at an impact momentum of 40.12 kg.m/s 88

Figure 35. Stress-time history of aluminum alloy 5083-H131 at an impact momentum of 24.9 kg.m/s 92

Figure 36. Stress-time history of aluminum alloy 5083-H131 at an impact momentum of 30.85 kg.m/s 93

Figure 37. Stress-time history of aluminum alloy 5083-H131 at an impact momentum of 40.12 kg.m/s 94

LIST OF TABLES

Table 1. Summary of Johnson Cook Coefficients from Quasi-static Data of Annealed Maraging Steel 300 55

Table 2. Summary of Dynamic Stresses gathered from experimental data for determination of the strain rate sensitivity coefficient C for Maraging Steel 300. 57

Table 3. Summary of Johnson-Cook Plasticity coefficients for Maraging Steel 300... 59

Table 4. Summary of Johnson-Cook Plasticity Coefficients for High Hardness Alloy 60

Table 5. Summary of Johnson-Cook Plasticity Coefficients for Aluminum Alloy 5083 63

Table 6. Summary of material parameters for Maraging Steel 300..... 66

Table 7. Summary of material parameters for High Hardness Armor..... 67

Table 8. Summary of material parameters for Aluminum Alloy 5083-H131..... 68

Table 9. Input parameters for ABAQUS 72

1. INTRODUCTION

1.1. Problem Statement

For years, engineers have been investigating new ways to improve the strength and reliability of metals and alloys for applications in a variety of fields from the aerospace industry and the military, to medicine and commercial uses. Vigorous testing in extreme conditions is necessary to understand the full extent of their behavior—whether it is in torsion, compression, or tension and at varying temperatures. Several experimental methods, devised to simulate the behavior of these metals under extreme conditions, exist—including, but not limited to, the Split-Hopkinson Pressure Bar apparatus and its variations, Taylor impact testing, flyer plate impact, and explosive ring testing. Further understanding of material behavior comes from grasping the knowledge of solid mechanics deeply rooted in dislocation theory, and using experimental results to verify this behavior for design.

Recent advances in computer technology have allowed the use of finite element codes to model and predict the behavior of materials under conditions of low and high strain rate deformation. Empirical models relying on experimental data or physical based constitutive relations based on dislocation mechanics have been developed and are widely used. Finite element modeling has evolved, yet has not been able to fully describe the behavior of these materials under all conditions. Recently there have been attempts to create more accurate material models that incorporate microstructural information. Questions, however, remain on how much of the microstructure has to be incorporated to

ensure accuracy. Although still in their infancy, several breakthroughs in predicting material behavior microscopically have been made.

A number of finite element codes have been developed today for commercial use—ANSYS and ABAQUS being two of the more popular ones. Both software packages can be used to solve problems ranging from simple linear analysis to advanced non linear simulations, including problems that involve static, dynamic, thermal, and electrical response of components. ABAQUS has been adopted as a popular finite element platform for use in the field of aeronautics and automotive engineering because it excels in simulating explicit dynamic time-dependent problems, such as blast, impact, and fracture mechanics applications.

The high cost associated with experimental work limits the size and number of specimens that can be tested. Furthermore, testing apparatuses do not provide direct information on the behavior of the specimens during deformation. Rather, they only capture information, such as energy absorbed by impact, or strains from sensors applied external to the specimen being tested. In some cases, high speed photography has also been employed to capture the deformation process qualitatively. Depending on the code used, finite element modeling can provide detailed information on the internal deformation of a specimen making it an extremely valuable tool for evaluating high speed deformation performance of metals.

Metals and alloys behave differently when subjected to high strain rate deformation compared to low or quasi-static deformation. They strain-harden and a considerable amount of heat is generated—softening the material. Under certain high

strain rate conditions, these metals exhibit high-temperature localized plastic shear caused by an imbalance between strain hardening and thermal softening. During this process, the amount of heat generated cannot escape due to the high strain rate deformation and becomes trapped in a localized region, plastically deforming the material and sometimes leading to a change in the microstructure and ultimate failure due to shear. This phenomenon is known as adiabatic shear band formation and has been known to be one of the leading causes of failure of metals under high strain rate conditions.

Adiabatic shear band formation in armor materials, for use in military applications, has recently become a primary source for concern among engineers. In the past, experimental testing has been the norm in determining the occurrence and severity of these bands under several conditions of high strain rate deformation. Recently, finite element modeling has been employed as a tool to predict these occurrences for the purpose of design using well-established models such as the Johnson-Cook empirical visco-plastic constitutive model and the Zerilli-Armstrong physical-based constitutive model. Despite the limitations in these models, they remain a staple in modeling the high strain rate behavior of metals.

1.2. Research Objectives

The objective of this research project was to simulate the behavior of armor metals at high strain rates and large strains, using the Johnson-Cook visco-plastic model, while incorporating the formation of adiabatic shear bands. The model was then to be applied to

three armor metals supplied by the Canadian Department of National Defense and tested at the University of Manitoba. To this end, the following steps were taken:

a) Conduct an extensive review of related literature dealing with behavior of metals under low and high strain rate deformation deeply rooted in dislocation mechanics; and gathering information on empirical and physical based constitutive models.
b) Build a finite element model based on Johnson-Cook visco-plastic constitutive equations, using the commercially available finite element program ABAQUS.
c) Evaluate the finite element model through comparison with experimental data for three armor materials in high strain rate compression: maraging steel 300, high hardness armor, and aluminum alloy 5083.
d) Identify failure modes and possible formations of adiabatic shear bands.

1.3. Research Methodology

To properly simulate the behavior of the three armor materials in high strain rate compression, a simplified version of the modified Split Hopkinson pressure bar was modeled into ABAQUS. Material libraries were constructed for each of the three armor metals. They incorporate constitutive equations that define both the elastic and plastic behavior during deformation. In addition to implementing the Johnson-Cook constitutive relations that define how the metals behave plastically, physical and thermal properties including simple isotropic elastic constitutive relations based on ASTM data, were

included. The Johnson-Cook dynamic failure model was added to simulate shear failure of the material, as a way of further describing the behavior of each of the materials at strain rates where adiabatic shear bands are more likely to develop.

Simulations at multiple impact momentums were performed for each of the materials. Results from experimentation conducted at the University of Manitoba were then used for comparison to ensure the accuracy and validity of the computations. To this end, an accurate mapping of the behavior of these metals over a range of impact momentums beyond the abilities of the apparatus could be obtained. Critical mechanical properties such as critical stress and strain at the moment of nucleation of shear bands and shear failure can be gathered and compared to known experimental results for the purpose of design.

1.4. Scope of Work

This thesis comprises of five chapters:

- Chapter one outlines the objectives of the research.

- Chapter two provides an overview of the background of plastic behavior of metals based on dislocation theory, starting with a basic understanding of simple crystalline structures and moving to the development of physical and empirical based constitutive relations used to describe the microscopic and macroscopic deformation of these materials subjected to various loading conditions—two of which are described in great detail. Theories related to high strain rate

phenomena, such as adiabatic shear band formation, are also addressed in this chapter as well as a summary of the current work in the field of microstructural finite element modeling of metals.

- In chapter three, experimental work dealing with high strain rate deformation of metals conducted at the University of Manitoba is reviewed.

- A detailed description of the finite element model developed to describe high strain rate compression of metals is provided in chapter four.

- Discussion of the results is presented in chapter five.

2. REVIEW OF RELATED LITERATURE

2.1. Deformation Mechanisms in Metals Based on Dislocation Mechanics

The mechanical properties of materials are a function of their microstructure. Properties such as grain size, particle or precipitate distribution and density of dislocations play an important role in the behavior of materials during deformation. Parameters including shear stress on a slip plane are dependent on the dislocation density within a crystal lattice of a material.

Most metals are crystalline whose constituent atoms are arranged in a pattern that repeats itself periodically in three dimensions. This pattern is defined by the crystal structure of the material. The most common structures are body-centered cubic (BCC), face-centered cubic (FCC), and close-packed hexagonal (HCP) structures, as shown in Figure 1.

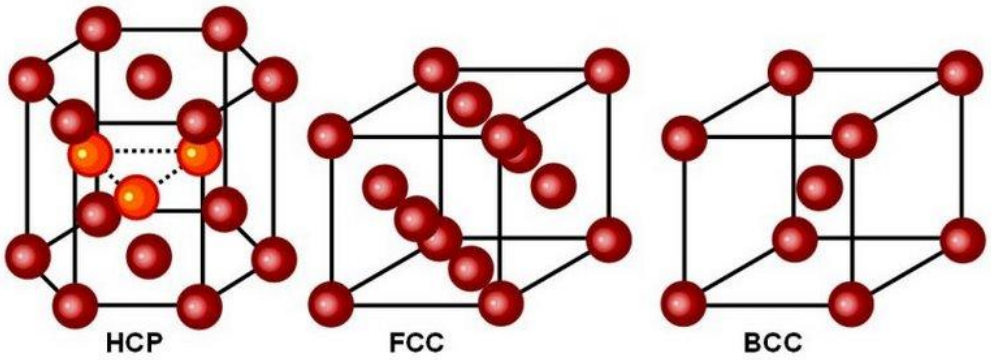

Figure 1. HCP, FCC, and BCC, unit cell structures

Examples of FCC metals include copper, silver, gold, aluminum and their alloys. The most notable BCC metals are steels, such as those used in armor plates.

The shear stress required to plastically deform a single crystal whereby atomic planes slide over each other was first developed by Frenkel in 1926 as follows:

$$\tau = \frac{Gb}{2\pi a} sin \frac{2\pi x}{b} \qquad \textbf{Eq. 2-1}$$

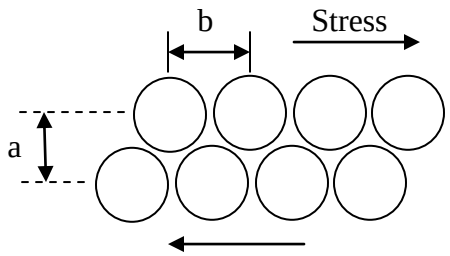

Figure 2. Slipping of two atomic planes in a simple crystalline structure

where τ is the applied shear stress, G is the shear modulus, 'b' is the spacing between atoms in the direction of the shear stress, 'a' is the spacing of the rows of atoms and x is the shear translation of the two rows away from the low-energy equilibrium position, as shown in Figure 2. This is related to the flow stress, or the shear stress necessary to induce plastic deformation in solid metals. This sliding motion creates dislocations in the original microstructure of the crystal.

Dislocations are a type of defect or imperfection within the crystal structure—also known as line defects. The presence of these defects alters the properties of the crystalline solids and disturbs the regular arrangement of the atoms. The glide of

dislocations results in slip which is the most common form of plastic deformation in solids, as shown in Figure 2. It is the successive sliding of one plane of atoms over another—i.e. slip planes. The climbing of dislocations is a phenomenon where dislocations move out of their slip planes. For example, when the dislocation line moves up one atom of spacing out of their original slip plane, the movement is called positive climb—which can occur by either diffusion of vacancies or the formation of an interstitial atom, as shown below in Figure 3 (Hull and Bacon 2001).

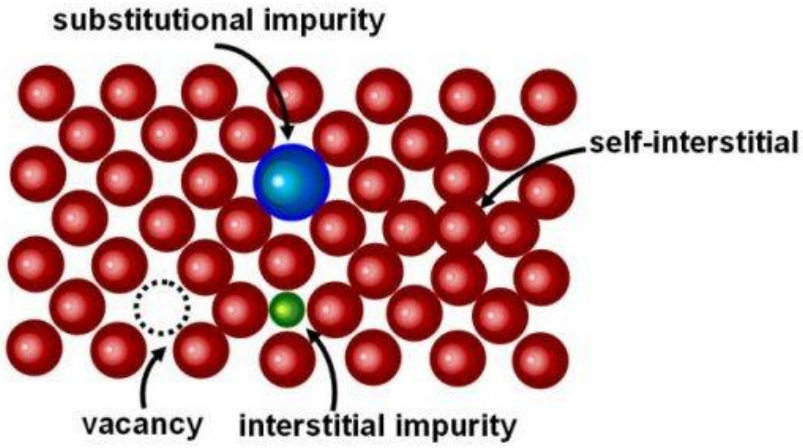

Figure 3. Types of point defects in a crystalline lattice

The most common types of geometry of dislocations can either be classified as *edge* or *screw*. Visual representations of both edge and screw dislocations for a simple cubic lattice structure are shown in Figure 4.

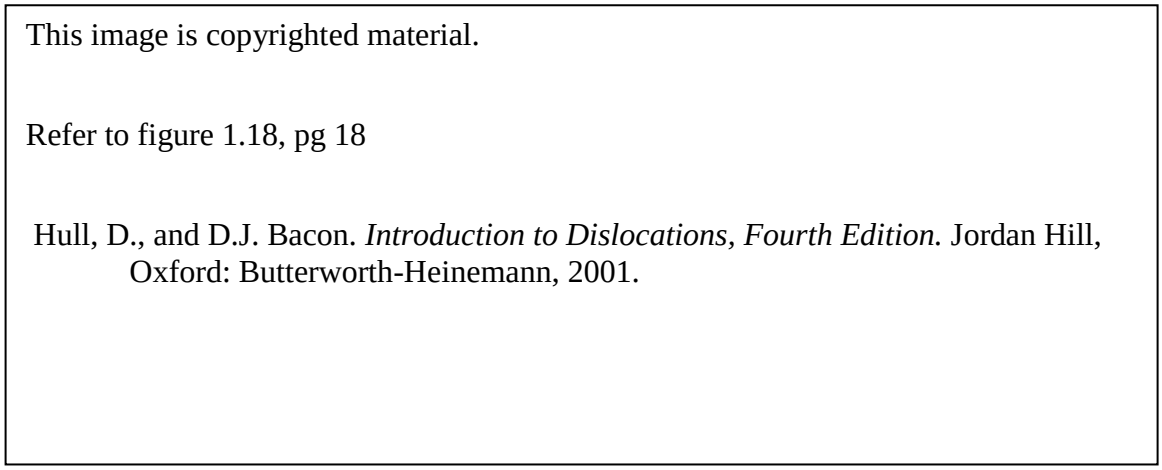

Figure 4. Positive edge dislocation and left-hand screw dislocation of a simple cubic lattice

The positions and orientations of dislocations are commonly described by the Burgers vector, named after Dutch physicist Jan Burgers. The Burgers vector, commonly labelled as "b", is defined as the magnitude and direction of the lattice distortion of dislocation in a crystal lattice (Callister 2005) and is shown in Figure 5.

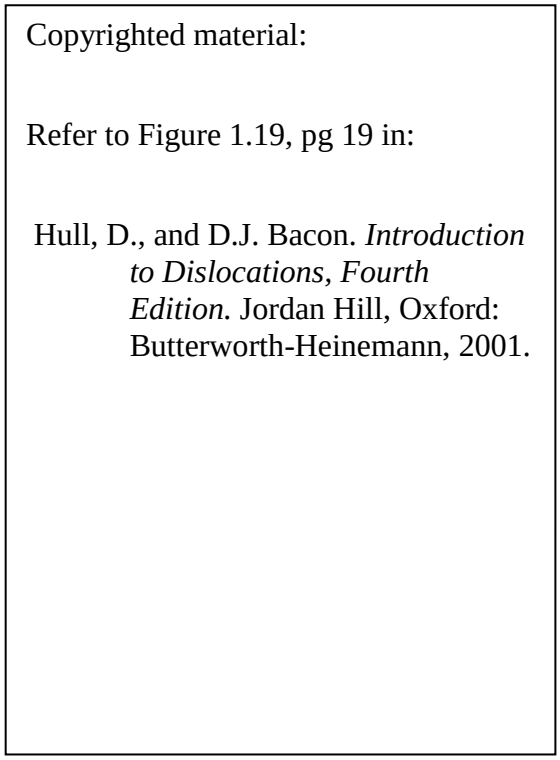

Figure 5. Burgers vector in a perfect crystal showing the lattice distortion of an edge dislocation(Hull and Bacon 2001)

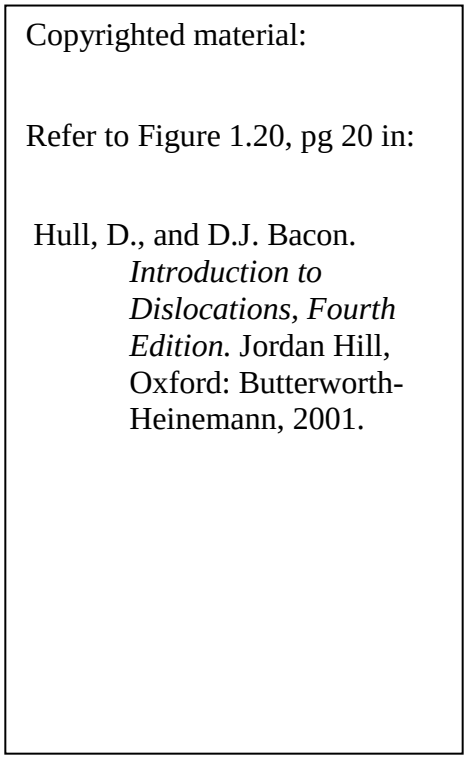

Figure 6. Burgers vector in a perfect crystal showing the lattice distortion of a screw dislocation(Hull and Bacon 2001)

For an edge dislocation the Burgers vector is normal to the line of dislocation and parallel for a screw dislocation. Parameters such as the strain energy of dislocations and the forces to move dislocations are dependent on the Burgers vector.

The applied resolved shear stress required to make a dislocation glide in a perfect crystal is known as the Peierls-Nabarro stress. It depends on the force-distance relationship between individual atoms and can be defined as the stress necessary for dislocations to move by one atomic space:

$$\tau_{PN} = \frac{Gb}{2c} \exp\left(\frac{-\pi a}{c}\right) sin\left(\frac{2\pi x}{c}\right) \qquad \textbf{Eq. 2-2}$$

where G is the shear modulus, b is the Burgers vector, c is the lattice spacing, and a is the lattice parameter. This stress follows the same concept as the one created by Frenkel (1926) and can be related to the critical shear stress required to move dislocations by gliding which ultimately induces plastic deformation in the material.

2.1.1. Plastic Deformation in BCC and FCC Metals:

Both BCC and FCC metals follow Hooke's Law when deforming elastically. However, there are different factors that affect the behavioral responses of these metals when they undergo plastic deformation. As mentioned earlier, plastic deformation involves the gliding of dislocations induced by applying stresses which surpass the critical resolved shear stress required to move dislocations. In metals, this deformation is controlled by the movement of dislocations past obstacles in the lattice caused by either increasing the applied stress or inducing thermal fluctuations (Thomson 2006, Rusinek, Rodriguez-Martinez and Arias 2009). This stress controls the macroscopic yield in materials.

In the 1950's Hall and Petch developed a series of equations that linked macroscopic yielding to the critical resolved shear stress for plastic deformation—basing their analysis on the pile-up of screw dislocations against obstacles in the lattice (Hall 1951, Petch 1953). They reported that when the macroscopic shear stress resolved onto the slip plane in the direction of the Burgers vector reaches a critical value, the

dislocation in the pile-up is able to push past the obstacle. They labelled this critical shear stress the Hall-Petch shear stress defined as:

$$\tau_{H-P} = \tau_o + \frac{k_{H-P}}{\sqrt{d}}; \qquad \textbf{Eq. 2-3}$$

where

$$k_{H-P} = \sqrt{\frac{\mu b \tau^*}{\pi}}\ , \qquad \textbf{Eq. 2-4}$$

τ^* is the obstacle strength, d is the spacing between obstacles, μ is the elastic shear modulus, b is the magnitude of the Burgers vector, and τ_o is the resistance to dislocation motion in a material free of obstacles ($d = \infty$). Materials with stronger obstacles have higher $k_{H\text{-}P}$ so that their yield strength and hardness is more sensitive to changes in d.

To measure this stress experimentally, a tensile test is required whereby a specimen is elongated at a constant rate (quasi-static) and the load on the specimen is measured simultaneously with the extension (Hull and Bacon 2001). The stress-strain behavior of ductile materials under tension and the resolved shear stress-strain are shown in Figure 7.

Figure 7. True tensile stress-strain curve of a BCC polycrystal and the resolved shear stress-strain curve of a single crystal (Hull and Bacon 2001)

The true tensile stress-strain curve is divided into four regions. In the elastic region the stress is proportional to the strain according to Hooke's Law, followed by micro-plastic deformation and yielding (E). This is then followed by a yield drop (EC) and subsequent yield propagation (CD), finally undergoing uniform strain hardening (DF). This work or strain hardening is a result of the increasing amount of flow stress required to maintain plastic flow in the material, reflected in the resolved shear stress vs. strain plot. Material parameters such as crystal structure, alloy composition, dislocation arrangement and grain size affect both the yield and flow stress.

2.2. Empirical and Physical Based Constitutive Models for Describing the Deformation Behavior of Metals

Early material models were very simple, at best including basic relationships between work hardening, strain rate dependence, and thermal softening. They defined the behavior of metals as having an elastic region with perfectly plastic behavior and a linear work hardening (Zerilli and Armstrong 1987). However, these models were only a numeric fit to test data and their accuracy was questionable outside the limited range of this data. To understand the thermo-visco-plastic behavior of metals during plastic deformation properly, a series of constitutive equations is needed. Development of material constitutive equations in the field of finite element modeling has evolved, driven by the need to improve efficiency of design in industries such as automotive, aeronautical, and military sectors. In their paper, Rusinek et al. (2009) categorize macroscopic constitutive modeling into two main groups:

a) Phenomenological Constitutive Models:

   These models provide a definition of the material flow stress based on empirical observations—consisting of mathematical functions with lack of physical background that fit experimental observations. They are characterized by a reduced number of material constants and easy calibration. They are used in restricted applications, covering a limited range of strain rate and temperature, and exhibit reduced flexibility for certain materials. Examples of this type of constitutive model include the Johnson-Cook Material Model.

b) Physical-based Constitutive Models:

These models account for the physical aspects of the material behavior—most grounded on the theory of thermodynamics and kinetic slip and dislocation theory (e.g. Zerilli-Armstrong Model (1987); Feng & Bassim's Model (1999)). These types of models tend to use a larger number of material constants and their determination procedure follows physical assumptions. They more accurately describe the material behavior under a wider range of loading conditions.

2.2.1. Physical-based Constitutive Models:

Most physical-based constitutive models created to describe the behavior of metals under plastic deformation at both low and high strain rates are based on dislocation-mechanics of the materials at the microstructural level. They take into account the factors that affect deformation and more specifically the resistance to deformation. These include: dislocations overcoming periodic lattice potentials, interactions between dislocations, interactions between dislocations and solute atoms, dislocations overcoming the long-range elastic stress field caused by grain boundaries, precipitates, dislocation forests, and other defects, as well as dislocations overcoming the viscous drag (Kapoor and Nemat-Nasser 2000). The obstacles within the material that must be overcome for plastic deformation can be categorized as either being short range or long range barriers. The former (thermal barrier) can be overcome by the application of thermal energy while the latter (athermal barrier) cannot.

In dislocation theory, the plastic shear strain rate $\dot{\gamma}$ is defined as:

$$\dot{\gamma} = \rho_m b m' v \qquad \textbf{Eq. 2-5}$$

where ρ_m is the mobile dislocation density, b is the magnitude of the Burgers vector, m' is the tensor orientation factor related to the distance the dislocation moves while overcoming the obstacle or barrier, and v is the average dislocation velocity (Orowan 1940). When the maximum dislocation velocity (which is close to the elastic shear wave speed) is exceeded, the strain rate becomes:

$$\dot{\gamma} = \dot{\rho_m} b m \Delta x \qquad \textbf{Eq. 2-6}$$

where $\dot{\rho_m}$ is the rate of increase of dislocation density and Δx is the average dislocation displacement whereby dislocations increase in density through nucleation rather than multiplication. (Gupta, Duvall and Fowles 1975).

At dislocation velocities lower than the elastic shear wave speed, v can be related to the shear stress-dependent Gibbs free energy of activation, which is the energy required to overcome thermal barriers within the material:

$$v = v_0 exp\left(-\frac{\Delta G}{kT}\right) \qquad \textbf{Eq. 2-7}$$

where v_o is the reference dislocation velocity, G is the Gibbs free energy of activation, k is Boltzmann's constant, and T is the absolute temperature. The plastic shear strain rate then becomes:

$$\dot{\gamma} = \rho_m b m' v_0 exp\left(-\frac{\Delta G}{kT}\right)$$ **Eq. 2-8**

Kocks et al. (1975) suggested an empirical relationship between the free energy of activation and the thermal shear stress resistance later used in the development of what is now known as the mechanical threshold model (Follansbee and Kocks 1988) given by the following expression:

$$\Delta G = F_0 \left[1 - \left(\frac{\tau^* \mu_0}{\hat{\tau}^* \mu(T)}\right)^p\right]^q$$ **Eq. 2-9**

where $0 < p \leq 1$ and $1 \leq q \leq 2$. In the above equation, τ^* is the shear stress required to overcome the thermal barrier at 0 K, and F_0 is the free energy required to overcome the barrier when the applied τ^* is zero. Through calculations and rearrangement of the above relations, the thermal shear stress resistance induced by the thermal barriers in the material can be expressed as:

$$\tau^* = \hat{\tau}^* \left[1 - \left(\frac{kT}{F_0} ln \frac{[\rho_m b m' v_0]}{\dot{\gamma}}\right)^{1/q}\right]^{1/p}$$ **Eq. 2-10**

The total shear stress resistance to plastic deformation is a combination of the thermal and athermal shear stress resistances in addition to the resistance due to viscous drag (Kapoor and Nemat-Nasser 2000). The athermal barriers are dependent on the microstructure of the material (grain size, dislocation density, and precipitates) which may or may not evolve with deformation. Thus,

$$\tau = \tau_{a1}(\rho) + \tau_{a2} + \tau^* \left[1 - \left(\frac{kT}{F_0} ln \frac{\left[\rho_m b m' v_0\right]}{\dot{\gamma}}\right)^{1/q}\right]^{1/p} + \tau_{drag} \qquad \textbf{Eq. 2-11}$$

This concept has also been extended to the case of uni-axial stresses and strains in a similar manner (Kapoor and Nemat-Nasser 2000):

$$\sigma = \sigma_{a1}(\rho) + \sigma_{a2} + \sigma^* \left[1 - \left(\frac{kT}{F_0} ln \frac{\dot{\varepsilon}_o}{\dot{\varepsilon}}\right)^{1/q}\right]^{1/p} + \sigma_{drag} \qquad \textbf{Eq. 2-12}$$

The athermal stresses, shown in Eq. 2-11 and Eq. 2-12, are denoted by subscripts "a_1" and "a_2", where a_1 are dependent on factors that evolve with deformation—i.e. dislocation densities and grain sizes and a_2 are dependent on factors that do not evolve with deformation, such as precipitates and solute atoms which rearrange themselves only through diffusion. These dislocation-mechanics based relations have been used specifically by Zurek et al. (1992) to model tungsten alloys and by Nemat-Nasser and Isaacs (1997) to model the constitutive behavior of tantalum at high strain rates. Nemat-Nasser and Li (1998) used the uni-axial case to model the constitutive behavior of copper at high strain rates with modification to include strain and temperature dependency on average dislocation spacing and dislocation densities.

Huang et al. (2009) have also been successful in modeling low and high strain rate deformation of FCC metals based on formulations derived above, by incorporating viscous drag effects and relating the entropy generation to the glide and accumulation of dislocations. They based their constitutive model on the theory of irreversible thermodynamics which is widely used in chemical and mechanical engineering but less so in physical metallurgy (Poliak and Jonas 1996). Poliak and Jonas used this theory to predict the initiation of dynamic recrystallization in nickels and steels (1996). This occurs when the entropy production rate reaches a minimum value and is based on the model developed by Ghoniem et al. (2000) to illustrate the motion of three dimensional interacting dislocation loops.

2.2.1.1. The Zerilli-Armstrong Physical-based Constitutive Model:

In 1987, Zerilli and Armstrong developed a series of physical based constitutive relations rooted in the theory of dislocations and extended the relations shown in Eq. 2-11 and Eq. 2-12 to distinguish between the specific mechanisms of plastic deformation in BCC and FCC metals. Their model was designed to describe the visco-plastic behavior of these metals at high strain rates. Similar to the dislocation model, Zerilli and Armstrong defined the flow stress as consisting of a thermal and an athermal part. The thermal part is defined as the stress necessary to overcome thermally activated dislocation barriers, increasing with increasing strain rate and decreasing with increasing temperature. The athermal part is represented as a power law relation of strain.

Zerilli and Armstrong (1987) were able to show that the distinguishing factor that affects the behavior of plastic deformation, between FCC and BCC metals, was that for FCC metals, increasing the strain increases the dislocation density and the thermal stresses are dependent on strain, strain rate and temperature. The thermal activation energy is also dependent on dislocation interactions (Basinski 1959). For BCC metals, the thermal activation energy is based on the movement of single dislocations (whose behavior is linked to the intrinsic Peierls-Nabarro stress, shown in Eq. 2-2) whereby the thermal stress portion is independent of the amount of strain. There is also a stronger dependence of the plastic yield stress on temperature and strain rate when compared to FCC metals.

The Zerilli-Armstrong constitutive equations, divided between FCC and BCC metals are shown in Eq. 2-13.

$$\sigma_{BCC} = \sigma_o + c_5\varepsilon^n + c_1 exp(-c_3T + c_4Tln\dot{\varepsilon})$$
$$\sigma_{FCC} = \sigma_o + c_5\varepsilon^n + c_2\varepsilon^{1/2} exp(-c_3T + c_4Tln\dot{\varepsilon}) \quad \textbf{Eq. 2-13}$$

where σ_o is a stress dependent on grain size and yield strength, $c_5\varepsilon^n$ is the athermal mechanism and the last set of terms is the thermal mechanism.

The limitation of this model lies in the fact that it cannot be used for strain rates that exceed the maximum dislocation velocity *v* which was defined earlier.

2.2.2. The Empirical Johnson-Cook Constitutive Model:

In many finite element programs for high strain rate deformation, the popular Johnson-Cook plasticity model is used. Being an empirical or purely phenomenological model, it is heavily dependent on experimental data; more so than the Zerilli-Armstrong constitutive model. Despite this, its parameters are more easily obtainable than those in physical-based constitutive models. The Johnson-Cook model is a Mises plasticity model with dependency on strain hardening law and strain rate; and is typically used in adiabatic transient dynamic simulations in conjunction with the linear elastic material model. It was developed in 1983 by Johnson and Cook (1985) to describe the behavior of several metals including Armco Iron, 4340 steel and OFHC copper during cylindrical impact loading.

2.2.2.1. Johnson-Cook Hardening Law:

Johnson-Cook hardening is isotropic, where the dynamic flow stress, σ_o, is assumed to be of the form:

$$\sigma_o = \left[A + B\left(\bar{\varepsilon}^{pl}\right)^n\right]\left(1 - \hat{T}^m\right) \qquad \textbf{Eq. 2-14}$$

where $\bar{\varepsilon}^{pl}$ is the equivalent plastic strain, A is the static yield strength, B is the strain hardening coefficient, n is the strain hardening exponent, m is the thermal sensitivity parameter and $\hat{T}$ is a non-dimensional homologous temperature defined as:

$$\hat{T} = \frac{\left(T - T_{ref}\right)}{\left(T_m - T_{ref}\right)} \qquad \textbf{Eq. 2-15}$$

The terms in the brackets of Eq. 2-14 define a power law relationship between true stress and effective plastic strain of the material. The term T_{ref} in Eq. 2-15 represents the ambient room temperature, and T_m is the melting temperature of the material. $\hat{T}$ is equal to zero when the temperature of the specimen is that of the ambient temperature and is equal to one when the temperature reaches melting.

2.2.2.2. Johnson-Cook Strain Rate Dependence:

Johnson Cook strain rate dependence assumes

$$\bar{\sigma} = \sigma_o\left(\bar{\varepsilon}^{pl}, T\right)R\left(\dot{\bar{\varepsilon}}^{pl}\right) \qquad \textbf{Eq. 2-16}$$

and

$$\dot{\bar{\varepsilon}}^{pl} = \dot{\varepsilon}_o exp\left[\frac{1}{C}(R-1)\right] \quad for \quad \bar{\sigma} \geq \sigma_o \qquad \textbf{Eq. 2-17}$$

where $\bar{\sigma}$ is the yield stress at non-zero strain rate; $\dot{\bar{\varepsilon}}^{pl}$ is the equivalent plastic strain rate; $\dot{\varepsilon}_o$ is known as the reference strain rate and is a material parameter; *C* is the strain rate sensitivity factor; and *R* is the ratio of the yield stress at non-zero strain rate to the static yield stress so that $R(\dot{\varepsilon}_o)$ = 1. There is a logarithmic dependence on strain rate. The Johnson-Cook representation of the dynamic flow stress is thus

$$\sigma_o = \left[A + B\left(\bar{\varepsilon}^{pl}\right)^n\right]\left[1 + Cln\left(\frac{\dot{\bar{\varepsilon}}^{pl}}{\dot{\varepsilon}_o}\right)\right]\left(1 - \hat{T}^m\right) \quad \textbf{Eq. 2-18}$$

2.2.2.3. The Johnson-Cook Dynamic Failure Model:

The Johnson Cook Dynamic Failure Model, suitable only for high strain rate deformation of metals, is used to model the initiation and progressive failure of metals, and is based on the value of the equivalent plastic strain at element integration points. Failure is initiated when the damage parameter exceeds one. The damage parameter, ω, is defined as

$$\omega = \sum\left(\frac{\Delta\bar{\varepsilon}^{pl}}{\bar{\varepsilon}_f^{pl}}\right) \quad \textbf{Eq. 2-19}$$

where $\Delta\bar{\varepsilon}^{pl}$ is an increment of equivalent plastic strain, $\bar{\varepsilon}_f^{pl}$ is the strain at failure, and the summation is performed over all increments in the analysis. The failure strain is assumed to be dependent on the non-dimensional plastic strain rate $\frac{\dot{\bar{\varepsilon}}^{pl}}{\dot{\varepsilon}_o}$; a dimensionless pressure-deviatoric stress ratio, *p/q* (where p is the pressure stress and q is the Mises stress); and the non-dimensional temperature $\hat{T}$, defined in the Johnson-Cook hardening model. The dependencies are assumed to be separable and are of the form

$$\bar{\varepsilon}_f^{pl} = \left[d_1 + d_2 exp\left(d_3\frac{p}{q}\right)\right]\left[1 + d_4 ln\left(\frac{\dot{\bar{\varepsilon}}^{pl}}{\dot{\varepsilon}_o}\right)\right]\left[1 + d_5\hat{T}\right] \quad \textbf{Eq. 2-20}$$

where d_1 through d_5 are failure parameters and $\dot{\varepsilon}_o$ is the reference strain rate. Most materials experience an increase in plastic failure strain with increasing pressure-deviatoric stress ratio. When the failure criterion is met the deviatoric stress components become zero.

2.2.2.4. Damage Initiation and Damage Evolution:

In most finite element codes, the Johnson-Cook plasticity model can be used in conjunction with the progressive damage and failure models. This allows the use of one or more damage initiation criteria including ductile, shear, forming limit diagram (FLD), forming limit stress diagram (FLSD), Müschenborn-Sonne forming limit diagram (MSFLD), and Marciniak-Kuczynski (M-K) criteria (ABAQUS Users' Manual 2008). After damage initiation, the material stiffness is degraded progressively according to the specified damage evolution response.

The models offer two failure choices, failure defined by a critical fracture energy or at a critical fracture strain while allowing the removal of elements from the mesh as a result of extreme element distortion. The progressive damage models allow for a smooth degradation of the material stiffness, making them suitable for both quasi-static and dynamic situations.

When used in conjunction with the dynamic failure models, damage evolution defines how the material degrades after one or more damage initiation criteria are met. Multiple forms of damage evolution may act on a material at the same time—one for

each damage initiation criterion that was defined. One can specify the type of damage evolution, either having a displacement damage evolution (defined as the damage as a function of the total displacement after damage initiation), or an energy damage evolution, whereby the damage is defined in terms of the energy required for failure, or total energy absorbed before failure (fracture energy).

2.3. Adiabatic Condition in Metals Subject to High Strain Rate Deformation and the Formation of Adiabatic Shear Bands:

The majority of metals are excellent heat conductors. When subject to deformation—either in tension, compression or torsion; heat is generated within the material. At low strain rates the heat generated will eventually dissipate over time and does not have a very large impact on the deformation properties of the material. However, at high strain rates, where deformation happens quickly, there is not enough time for the heat to dissipate from the localized area of deformation. The heat becomes trapped resulting in a localized temperature rise—thermally softening the material and leading to a localized change in the microstructure of the material and possible eventual failure. The shear resistance in this localized region of the material is subsequently reduced—leading to the formation of adiabatic shear bands, or ASB's. Two types of ASB's exist, deformed bands and transformed bands.

In a sense, shear bands form when the effect of thermal softening in a localized region of the material outweighs the effect of strain hardening. They tend to nucleate outwards from the source of mechanical instability. Recht (1964) first developed a

correlation between shear band nucleation and shear strain where the slope of the adiabatic stress-strain curve is zero. Further analysis of shear band nucleation was later carried out by Clifton et al. (1984) via the formulation of simple linear perturbation analysis. Studies have shown that in some cases many shear bands will form parallel to each other if two nucleation points of similar size and type are within close proximity of each other (Campbell 1973). In his thesis, Cepus (1995) claimed that nucleation points can either be at locations of precipitates, phase boundaries, voids present in the material, scratches, machine marks or thin sections in the material and that macroscopic flaws act as stress concentrations which results in more heat generation and thermal softening in the region close to the flaw.

High strain rate experiments for impact of steel projectiles into titanium alloy plates performed by Grebe and Meyers (1985) and by Kuriyama and Meyers (1987) have shown that the width of shear bands can range from anywhere between one and 100 μm.

Under certain conditions, the localized zones in the material may undergo phase transformations and experience permanent changes in microstructure. These shear band areas are known as transformation bands, or white-etching bands due to their white appearance under a scanning electron microscope, and the temperature within the bands is much higher than in the deformed bands by several hundred degrees. Upon completion of plastic deformation these shear bands are quenched by the surrounding matrix resulting in the formation of a highly reflective microstructure which appears as a white band under optical microscopes. Materials that undergo phase transformations at elevated temperatures tend to be ideal for the nucleation of transformed bands (Campbell 1973, Cepus 1995).

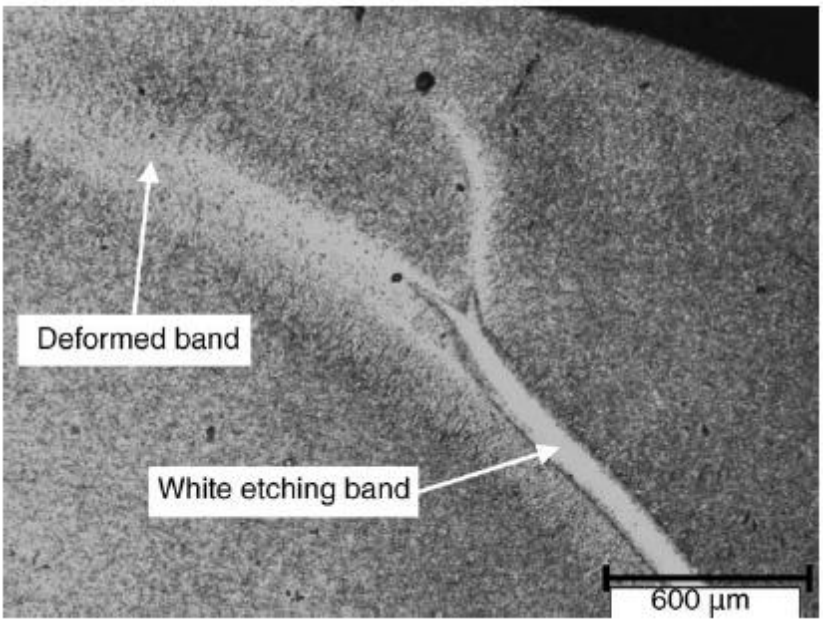

Figure 8. Optical micrograph showing white etching band and deformed band in the microstructure of AISI 4340 steel after impact (A. Odeshi, M. Bassim, et al. 2005)

Studies have shown relations between the formation of adiabatic shear bands and specific properties of materials. Materials with low thermal diffusivities and critical longitudinal strain such as steels and Ti alloys have a higher tendency to form transformed shear bands compared to softer materials with higher thermal diffusivities such as Copper and Aluminum, which tend not to form any bands (Campbell 1973). Bassim and Panic proposed that the stress drop at yielding for high strength low alloys steels under high strain rate deformation is the result of adiabatic shear band formation caused by dislocation pileups at grain boundaries which are pinned strongly by solutes (Armstrong and Zerilli 1994, Bassim and Panic 1999). The upper yield stress is related to the large stress needed for dislocations to break free and the lower yield stress corresponds to the stress needed for the dislocations to continue moving unhindered. In

his thesis, Thomson (2006) claimed that materials that have a high microstructural stress intensity factor and low thermal conductivity are more prone to shear band formation. This is one explanation to why BCC metals are more prone to shear band formation than FCC metals. Cepus (1995) also reported that a material with high strain rate sensitivity and low strain hardening rate will become unstable at high strain rates and ultimately fail through the formation of an adiabatic shear bands. Backman and Finnegan (1973) have shown that under certain strain rates, pearlitic/ferritic microstructures tend to show more deformed shear bands, while tempered martensitic microstructures form more transformed shear bands.

2.4. Mechanical and Thermal Instabilities during High Strain Rate Deformation:

As discussed previously, thermal mechanisms such as adiabatic conditions and thermal softening play a predominant role in the deformation behavior of metals at high strain rates. While normally negligible at low loading conditions, these along with inertial forces contribute to instabilities that form within the material leading to possible nucleation of adiabatic shear bands and ultimate failure. In 1944, Zener and Holloman introduced the concept of thermal softening whereby adiabatic shearing forms when the loss of strength due to heating exceeds the gain in strength due to strain hardening (Zener and Hollomon 1944, Baron 1956, Backofen 1964, Culver 1973, Argon 1973, Staker 1981). During deformation, work hardening raises the flow stress while heat begins to build causing the flow stress to fall. Instability starts when the rate of softening first

exceeds the rate of hardening. A high strain rate compression test is said to be adiabatic if the strain rate is sufficiently high so that no heat is lost during the test. The thermal and mechanical instabilities that lead to the formation of adiabatic shear bands, are described in more detail below.

The microstructural instabilities in metals that arise during high strain rate deformation can be described through dislocation mechanics. Rather than simple uniform plastic deformation, instabilities arise when there is an adiabatic localization of plastic shear in the material, which may lead to shear failure. In general, the flow stress of a material, σ_o, depends on the strain, strain rate, and temperature. That is:

$$\sigma_o = \sigma_o(\varepsilon, \dot{\varepsilon}, T) \qquad \textbf{Eq. 2-21}$$

Instability occurs when $d\sigma_o = 0$, or:

$$\left(\frac{\partial \sigma_o}{\partial \varepsilon}\right)_{T,\dot{\varepsilon}} d\varepsilon + \left(\frac{\partial \sigma_o}{\partial T}\right)_{\varepsilon,\dot{\varepsilon}} dT + \left(\frac{\partial \sigma_o}{\partial \dot{\varepsilon}}\right)_{\varepsilon,T} d\dot{\varepsilon} = 0 \qquad \textbf{Eq. 2-22}$$

which can also be written in terms of shear strains as:

$$\left(\frac{\partial \tau_o}{\partial \gamma}\right)_{T,\dot{\gamma}} d\gamma + \left(\frac{\partial \tau_o}{\partial T}\right)_{\gamma,\dot{\gamma}} dT + \left(\frac{\partial \tau_o}{\partial \dot{\gamma}}\right)_{\gamma,T} d\dot{\gamma} = 0 \qquad \textbf{Eq. 2-23}$$

If full adiabatic conditions are assumed along with negligible changes in strain rate during deformation (constant strain rate) all plastic work is converted into heat and the above equation becomes:

$$\left(\frac{\partial \sigma_o}{\partial \varepsilon}\right)_{T,\dot{\varepsilon}} = -\left(\frac{\partial \sigma_o}{\partial T}\right)_{\varepsilon,\dot{\varepsilon}} \frac{dT}{d\varepsilon} \qquad \textbf{Eq. 2-24}$$

This condition states that at the onset of instability, strain hardening is equal to thermal softening. The left hand side of Eq. 2-24 represents the effect of strain hardening while the right hand side represents thermal softening. Once thermal softening outweighs the effects of strain hardening, adiabatic shear bands may form. Instability stresses, strains, and temperatures can easily be identified from experimental results of true stress-strain diagrams. However, predicting these theoretically takes significant effort. Dodd and Atkins were able to derive the instability criterion based on the maximum shear stress criterion taking into account the void growth and its influence on thermal softening (Dodd and Atkins 1983, Panic 1999). Others have been able to identify the instability strain based on the maximum stress criterion using linear strain hardening with yield strength constitutive equations (Bai 1981, Staker 1981, Olson, Mescal and Azrin 1981); power law with yield strength equations (Lindholm and Johnson 1983); and power law without yield strength considerations (Culver 1971, Vinh, Afzali and Roche 1979, Olson, Mescal and Azrin 1981, Burns, Grady and Costin 1982).

In his paper, Bai (1981) defined the instability at onset of adiabatic shear localization by taking into account the degree of inhomogeneities at different locations in the material and then comparing them to uniform bodies without defects. His criterion says that if the inhomogeneity is not amplified, there would be no localization. This inhomogeneity is defined as:

$$\frac{\Delta ln\dot{\gamma}}{\Delta ln\gamma} = \chi \qquad \textbf{Eq. 2-25}$$

where Δ refers to the difference between the inhomogeneity and the uniform body. Solving Eq. 2-25 with respect to time yields:

$$\frac{\Delta\gamma}{\Delta\gamma_o} = \left(\frac{\gamma}{\gamma_o}\right)^{\chi} \qquad \textbf{Eq. 2-26}$$

$$\frac{\Delta\gamma}{\gamma} = \left(\frac{\gamma}{\gamma_o}\right)^{\chi-1}\frac{\Delta\gamma_o}{\gamma_o} = k(\gamma)\frac{\Delta\gamma_o}{\gamma_o} \qquad \textbf{Eq. 2-27}$$

where k(γ) is the amplification factor of relative localization. If a simple power law relation of shear flow stress is assumed without dependence on yield strength, i.e. $\tau = A\gamma^n\dot{\gamma}^m T^{-\nu}$, keeping in mind that for simple shear the cross sectional area of the body remains constant, the application of the above relation becomes:

$$\frac{\Delta\tau}{\tau} = \mathrm{m}\frac{\Delta\dot{\gamma}}{\gamma} + \mathrm{n}\frac{\Delta\gamma}{\gamma} - \nu\frac{\Delta\mathrm{T}}{\mathrm{T}} = 0 \qquad \textbf{Eq. 2-28}$$

The amplification factor, k, in Eq. 2-27 must be greater than one (unity) for localization to occur. Instability occurs for χ=1. Substituting this back into Eq. 2-27 and then into Eq. 2-28, rearranging to solve for the instability strain, produces:

$$\gamma_i = \frac{\left(\frac{(m+n)T}{\nu}\right)}{\frac{dT}{d\gamma}}$$ **Eq. 2-29**

This instability strain includes strain rate sensitivity and separates dependencies on strain hardening effects and strain rate sensitivity unlike the instability strain derived from maximum stress criterion for the same power law relation:

$$\gamma_i = \left\{ \frac{n\tau}{A\nu\left(\frac{dT}{d\gamma}\right)} \frac{T^{\nu+1}}{\dot{\gamma}^n} \right\}^{1/(n+1)}$$ **Eq. 2-30**

In reality there are several factors that contribute to the formation of adiabatic shear bands including, but not limited to: density of the material, specific heat, thermal diffusivity, strain hardening factor, thermal softening factor, strain rate sensitivity factor, strain rate, shear stress, shear strain, grain size, and crystallographic orientation. Complete adiabatic conditions are ideal but do not exist in reality. If the former were to be true, thermal diffusivity of the metal would be zero. In fact, as thermal conditions approach adiabatic conditions, the thermal diffusivity would approach zero, and the material would be more susceptible to adiabatic shear band formation. Metals with lower thermal diffusivities are more susceptible to adiabatic shear band formation, which was discussed earlier (Cepus 1995, Panic 1999).

Extending this theory to more complicated constitutive relations, such as Johnson-Cook and Zerilli-Armstrong models alike, requires the use of computational finite

element programs. Although not explicitly defined in the constitutive models, localization effects can be simulated by forcefully inducing thermal and mechanical instabilities in the material to the desired effect. This method has been used by Feng and Bassim (1999) in their development of physical based constitutive relations for metals at high strain rates.

2.5. Current Research in the Field of Microstructural Finite Element Modeling of Metals

Recent advances in computer technology have allowed the use of finite element modeling to predict the behavior of materials under certain predetermined conditions for high strain rate deformation. Current work includes, but not limited to, finite element modeling of the mechanical behavior of steels under high strain rate deformation to predict the formation of adiabatic shear bands (Feng and Bassim 1999). Feng & Bassim used ANSYS to model the formation and behavior of adiabatic shear bands in AISI 4340 steel for the purpose of determining the treatment and material properties on of the ASB's. In their model, instabilities required for the formation of shear bands were thermally and mechanically induced to the desired effect, and their constitutive relations defined the behavior of the material subjected to the induced shear bands. Experimental results were used to verify the accuracy of their analysis.

Recently, there have been attempts to create more accurate material models that incorporate information of the microstructure of the material in an attempt to predict the

mechanical behavior of materials microscopically (Becker and Richmond 1993, Gosh, Lee and Moorthy 1996, Smit, Brekelmans and Meijer 1998).

In the development of these models, questions arose on how much detail on the geometry of the microstructure had to be incorporated to ensure accuracy. Generally, material models would only predict the mechanical behavior of the materials based on the mean values of microstructural information such as crystallographic orientation distribution functions, porosity or second-phase volume fraction, but not use any information on the geometry of the microstructure (Becker and Richmond 1993). Hunt et al. (1987), Magnusen (1987), and Blicharski et al. (1993), have shown through experimental evidence that detailed information on the geometry of the microstructure was important to accurately model phenomena such as recrystallization, shear localization and fracture.

Although relatively successful in predicting the evolution of crystallographic orientations, polycrystalline deformation models have shown that it is difficult to track individual grains in finite deformations in the polycrystal (Becker and Richmond 1993). Smelser and Becker (1989) developed a polycrystalline model that is based on crystal constitutive relations coded in user-subroutines and modeled using the finite element code ABAQUS. This model was only successful in predicting the crystal orientation of several grains which experienced little or no orientation change under certain compressive strains. Only for these grains did the model correctly predicted the relative stability of their orientation. Smelser and Becker also developed a model for pore distribution for ductile fracture of materials tested under tension by Magnusen et al. (1988) and a model for second-phase distribution based on experiments conducted by

Brockenbrough et al. (1992) who investigated the relationship between particle cracking and critical stress in particles, using tensile specimens.

Most empirical and physical based constitutive models require large amounts of experimental data to validate their accuracy. Dynamic stress response data gathered by performing experiments on specimens, both at low and high strain rates and often at multiple temperatures, are also used as a basis for development of these models. High strain rate experimentation conducted at the University of Manitoba over the last two decades was reviewed and experimental data were gathered to build the constitutive finite element model used in this research study.

3. HIGH STRAIN RATE EXPERIMENTATION

There are many techniques developed to capture the behavior of materials subjected to high strain rate conditions. These include tests conducted under high strain rate compression, tension, and torsion. Below is a representation of various loading conditions and testing considerations for metals undergoing deformation under increasing strain rates:

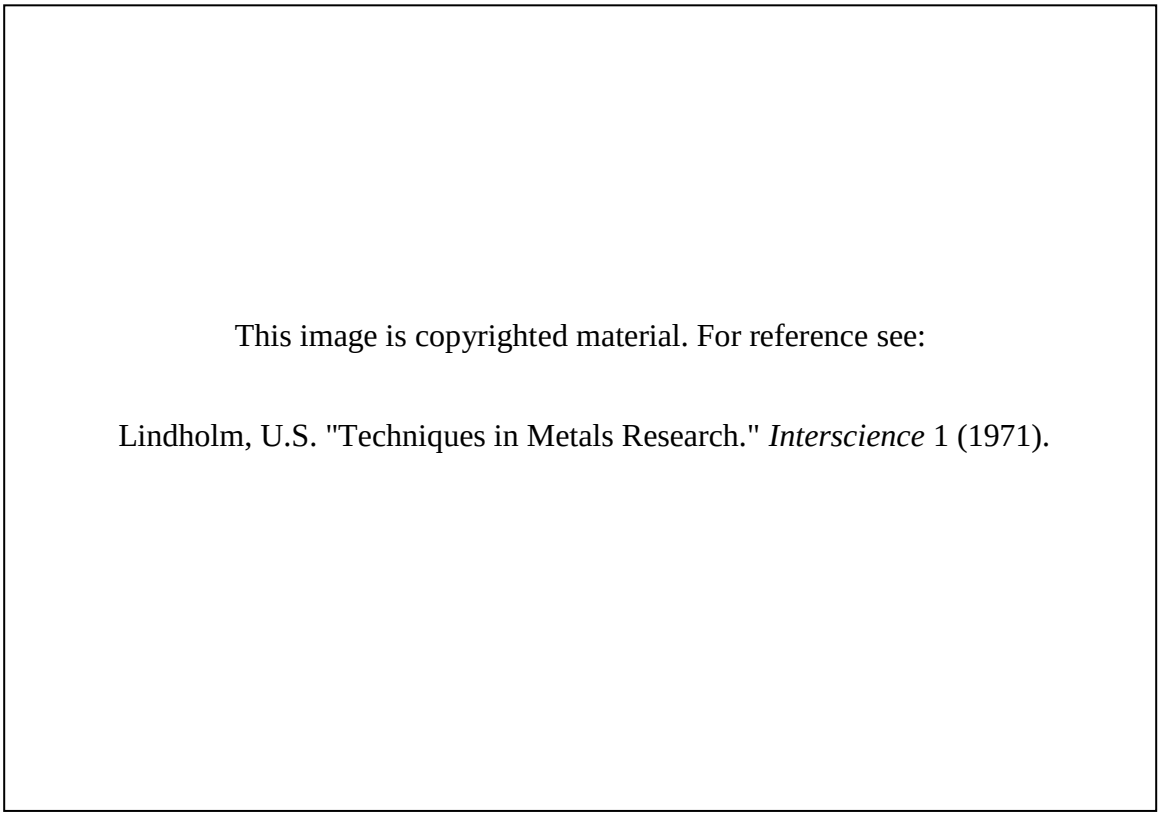

Figure 9. Method of loading and dynamic considerations for metals deformed at various strain rates (U. Lindholm 1971)

Examples of high strain rate testing include the rod impact test first performed by Taylor and Whiffen (1948) by accelerating cylindrical specimens into rigid plates resulting in shortened rods due to plastic deformation. Variations to this impact test, include two rods impacting onto each other. Other tests, such as the expanding ring test, are based on a sudden detonation of an explosive charge at the center of a ring. This test subjects specimens to tensile loads with strain rates in excess of 10^4 s^{-1} and provides full high strain rate stress-strain relationships for the test specimen (Campbell 1973). The flyer plate impact tests involve a flat plate slamming at high speeds into a stationary target plate. Data from these experiments provide high strain rate yield-stress, shockwave response, spall strength and equations of state information for materials undergoing uni-axial strain.

The most notable and more widely used test method is the Split Hopkinson Pressure Bar (SHPB) and its variation, the Torsional Split Hopkinson Pressure Bar (TSHPB). The SHPB apparatus was based on devices invented by Bertram Hopkinson and Herbert Kolsky and was developed by Dr. Ulric Lindholm at Southwest Research Institute, San Antonio Texas, in 1962. Its purpose was to evaluate the behavior of metals under various conditions at high strain rates (impacts and explosions) (The American Society of Mechanical Engineers 2006). Applications include determining the dynamic strength of steel in offshore platforms subjected to impact, defining the compressive strength of ceramics used in advance armors, evaluating pipeline and nuclear pressure vessel steels, and evaluating the strength of materials on the pressurized hulls of the U.S. space station under impact from meteorites or other orbital debris impact. A schematic of the two-bar Split Hopkinson apparatus is shown in Figure 10.

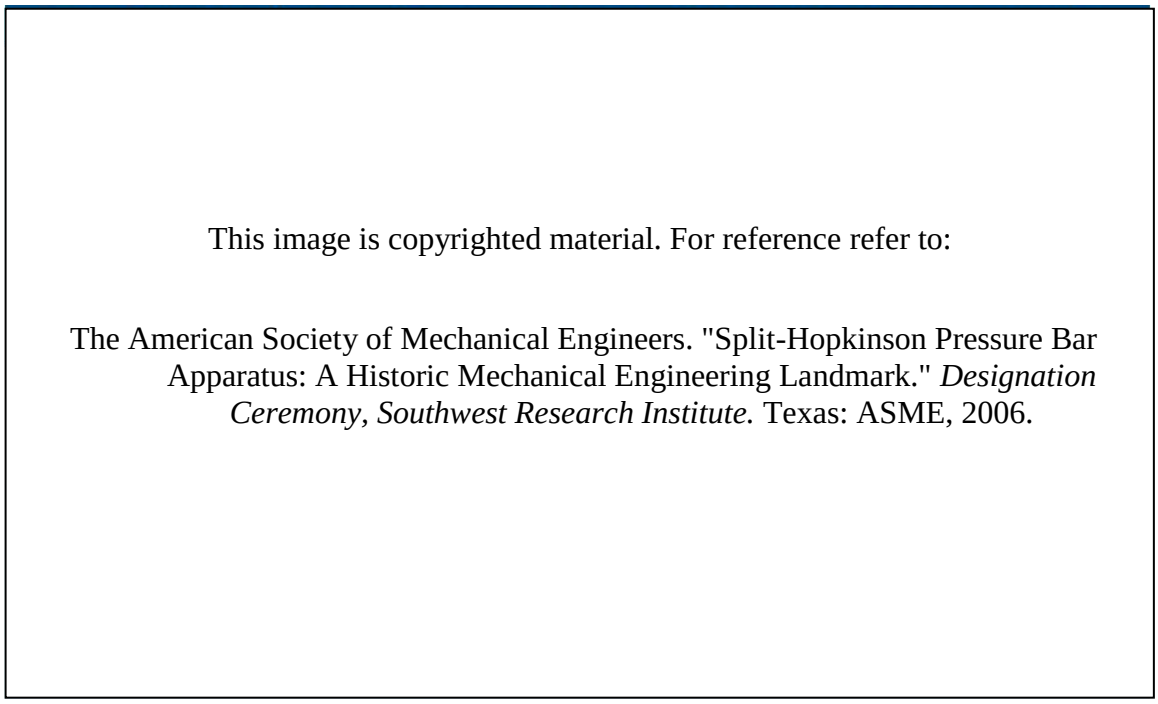

Figure 10. Schematic of Split Hopkinson Pressure Bar (The American Society of Mechanical Engineers 2006)

Information from the SHPB test specimens is derived indirectly from the wave magnitude signals entering and leaving the specimen via strain gages placed throughout the apparatus. The difference between total input and total output represents the amount of load signal required to deform the specimen (Campbell 1973). Incident, transmitted, and reflected waves are recorded by these strain gauges and then translated into data that can be used to calculate the stress strain relationships of the specimen. The torsional split Hopkinson bar works in a similar fashion and is used to gather shear stress and strain data, otherwise impossible with the normal apparatus. A schematic of this system is shown in Figure 11.

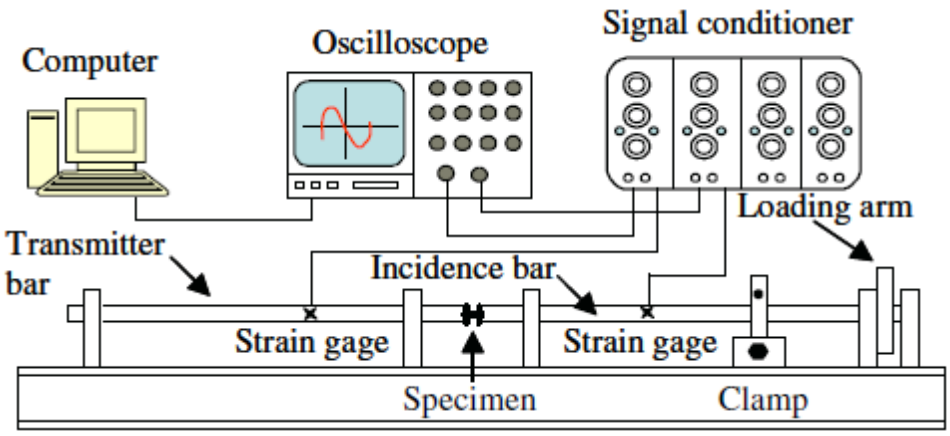

Figure 11. Torsional Split Hopkinson Pressure Bar Apparatus (Yazdani, Bassim and Odeshi 2009)

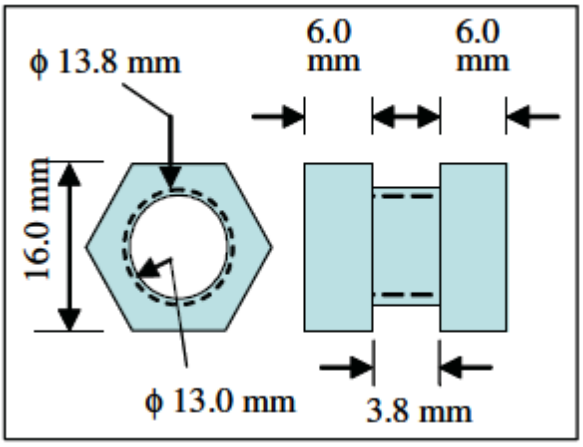

Figure 12. TSHPB Specimen Schematics (Yazdani, Bassim and Odeshi 2009)

3.1. Experimental work conducted at the University of Manitoba

Prior to 1990, high strain rate experimentation was performed to understand the basic behavior of metals at varying conditions of stress, strain, and strain rate. The majority of existing apparatuses used to this end have produced fairly accurate stress-strain profiles of deformed specimens showing the effects of strain hardening and thermal softening. The Split Hopkinson Pressure Bar has been used to show maximum compression and tension stresses while the Torsional Split Hopkinson Par has been used for shear stress analysis. However, due to the limitations of many of these apparatuses it was impossible to reproduce conditions conducive to shear band formation.

Adiabatic shear bands usually develop at conditions of high strains and high strain rates. However, the real-world conditions necessary to form these bands were not well known and could not be reproduced in any experimental setting.

In the early 1990's, a modified version of the Split Hopkinson Pressure bar was developed (Nakkalil, Hornaday Jr. and Bassim 1991), removing the two-bar system, and allowing direct impact of the projectile bar onto the specimen. Thus, it became possible to achieve greater strains and strain rates. A schematic of this modified, or direct impact, Split Hopkinson Pressure Bar apparatus is shown in Figure 13.

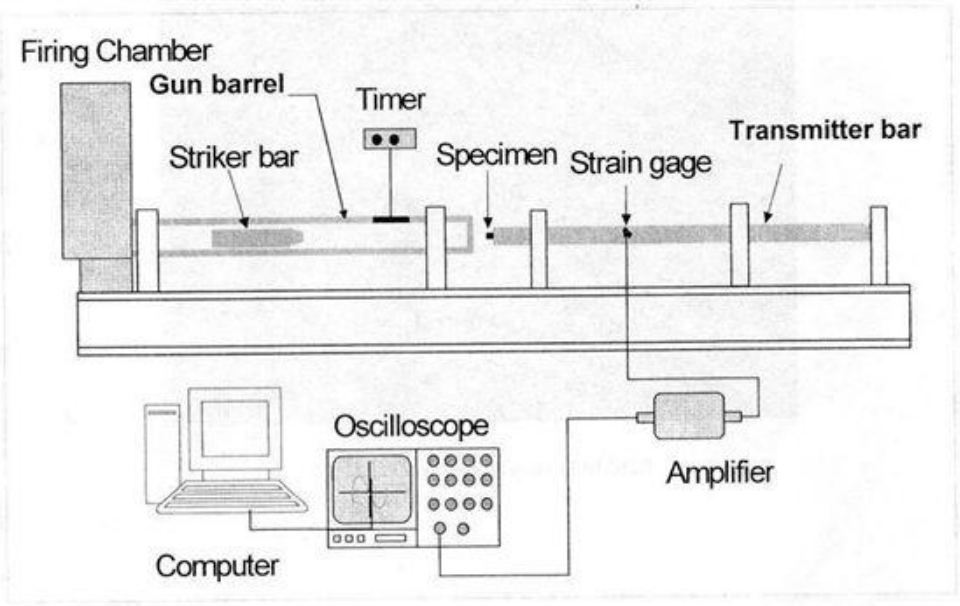

Figure 13. Direct Impact Split Hopkinson Pressure Bar used at The University of Manitoba (Mirfakhraei 2008)

As shown in Figure 13, the equipment consists of a light gas gun used to fire the projectile, a transmitter bar 3.8 cm in diameter and 1.5m long, strain gauges, a strain pulse amplifier, a storage oscilloscope and a computer. The light gas gun is operated using compressed air. Varying the pressure of the air in the cylinder allows for variation in the velocity of the projectile. The projectile is machined from a cylindrical 4340 steel bar and heat treated to 45-50 HRC. It is 0.2m long and 3.8 cm in diameter. The transmitter bar is made of 4340 steel at 45 HRC. Strain gauges are mounted on the surface at a distance of 30 cm from the impact-receiving end. The transmitter bar is held in position by steel supports and shock absorbers are in place at the end of the bar. The length of the transmitter bar was designed in such a way that the time taken for the reflected pulse to arrive at the strain gauges would be greater than the time required for

the deformation of the specimen. This ensures uninterrupted recording of the loading pulse.

Nakkalil et al. (1991) used the direct impact version on the Hopkinson Pressure Bar apparatus to conduct dynamic compression tests to describe the mechanical behavior of four different plain carbon and low alloy eutectoid rail steels at elevated temperatures between 25-680°C and strain rates exceeding 10^3 s^{-1}. Adiabatic stress-strain curves were generated and it was found that the flow stress dependencies on the initial testing temperature at high strain rates follow the same established trends reported for low strain rates. Impact at low deformation temperatures (25-180°C) was found to induce localized catastrophic shearing at high strain rates for steels with a fine pearlitic structure.

In his thesis, Cepus (1995) investigated the high strain rate behavior of metals in torsion using the Torsional Split Hopkinson Bar apparatus, shown in Figure 11, which was designed, built and tested at the University of Manitoba specifically for use in his experiments. Two series of experiments were conducted—one at room temperature and the other at -30°C. Test specimens were made from SPS-Plus steel at five different heat treatments and hardness. Analysis was then conducted to determine the relationship between selected material parameters and material hardness. Cepus also investigated the possible nucleation of adiabatic shear bands as a cause for shear failure and analysed the size of the adiabatic shear band relating it to the strength of the material. Cepus found that all of the specimens tested were very ductile except for the steel tempered at 640°C which formed transformed shear bands.

Panic (1999) used the same TSHPB apparatus to test AISI 4140 steel at three different strain rates for the purpose of developing a relationship between adiabatic shear band formation and geometry with respect to strain rate. He found that the higher the strain rate, the narrower the width of the shear band, and the harder the material. Panic also investigated the influence of material hardness on the failure mechanisms by testing multiple tempers and hardness of 4140 steel. All of his specimens showed some adiabatic shear band formation. He concluded that depending on the strain rate, some specimens showed deformed shear bands and some showed transformed bands. By using a scanning electron microscope (SEM), it was determined that all specimens fractured in a ductile manner rather than brittle as was expected at higher strain rates, and that the strain rate and hardness did not have an impact on the type of fracture, but rather had an effect only on the characteristics of fracture.

In 2005 Al-Ameeri investigated the effects of heat treatment on adiabatic shear bands which formed in 4340 steel by direct impact loading using the direct impact Hopkinson Pressure Bar apparatus shown in Figure 13. The adiabatic shear bands were found to be very hard and brittle and exhibited a tendency to brittle fracture. Various heat treatments were applied to specimens which formed adiabatic shear bands. Annealing the shear bands was performed at 315°C for two hours and at 650°C for 20 minutes and for 2 hours as well. At 315°C heat treatment did not produce any considerable effect on the microstructure and hardness of the adiabatic shear band. Annealing at 650°C for 20 minutes significantly reduced the hardness of the shear band to the same level as the bulk of the material outside the shear band. Extending the annealing time to two hours at 650°C led to a change in the microstructure of the transformed band from a white brittle

formation to a more ductile deformed band that is observable within the magnification of an optical microscope. It was concluded that the microstructural changes that occur during adiabatic shearing can be reversed by heat treatment (Al-Ameeri 2005, Odeshi, Bassim and Al-Ameeri 2006).

Yazdani et al. (2009) first observed adiabatic shear bands in commercial pure copper (99.94% Cu) subjected to high strain rate torsion in excess of 10^3 s^{-1}. The formation of shear bands, particularly narrow deformation bands, in copper had been questioned due to the metal's ductility and its ability to exhibit uniform deformation at relatively large strains. Shear band occurrences were measured as a function of initial torque and angle of twist of the specimens in the torsional split Hopkinson Bar apparatus. It was concluded that these bands can be induced in ductile materials such as polycrystalline copper and the source of these bands is correlated to the extensive shear deformation before fracture.

In her thesis, Mirfakhraei (2008) investigated the deformation behavior and modes of failure at high strain rates of three armor materials: rolled homogeneous alloy (RHA), aluminum 5083, and Tungsten A 90S using the direct impact Hopkinson Pressure Bar apparatus shown in Figure 13. Dynamic stress-strain curves were generated for each of the materials at varying strain rates and the specimens were subjected to microscopic evaluation to determine the microstructural evolution during deformation. The objective was to determine the failure and deformation mechanisms under extreme loading conditions as in the case of ballistic impact. Experimental results showed that the thermo-mechanical instabilities leading to the strain localization and occurrence of adiabatic shear bands dominate the deformation and failure mechanism of these materials at high

strains and strain rates. Deformed bands were observed in both tungsten and aluminum alloys. The ultimate flow stress in tungsten and RHA increased as impact momentum increased until a critical value conducive to adiabatic shear band formation was reached, after which the ultimate flow stress fell. However in aluminum alloys it was seen that there was no significant change in maximum flow stress as impact momentum was increased, showing a clear distinction in the factors that affect plastic behavior in both BCC and FCC metals.

In 2009, three new armor materials, provided by the Canadian Department of National Defence were tested: Maraging Steel 300, High Hardness Armor (HHA), and Aluminum 5083. The direct impact Split Hopkinson Pressure Bar and the variational Torsion Split Hopkinson Pressure Bar were used by Ghaznafar Nazimuddin, an MSc. candidate at The University of Manitoba (2010), to determine the effect of impact momentum on the deformation behavior and failure mechanisms of these materials in compression and torsion. Testing was conducted at various impact momentums and degrees of twisting for the purpose of obtaining dynamic stress-strain curves. Any shear band formation was recorded to determine the factors that affect their occurrence such as critical impact momentum, strain, shear stress, maximum compressive stress.

In this thesis, dynamic stress-time plots for three armor materials—maraging steel 300, high hardness armor (HHA), and aluminum alloy 5083—produced through modelling, were compared to the experimental results obtained by Nazimuddin (2010) in order to verify the validity of the theoretical model. Development of the model, using the Johnson-Cook constitutive relations, was compared to experimental stress-strain responses of specimens subjected to varying strain rates using the direct impact split

Hopkinson Pressure Bar (SHPB). A complete review, showing the development and application of the model is given in the following sections.

4. FINITE ELEMENT MODELING

4.1. Introduction

Due to its flexibility and ease of use in finite element software, such as ANSYS and ABAQUS, the visco-plastic Johnson-Cook material model is implemented to predict the behavior of armor metals under high strain rate compression. This model provides a basic representation of the behavior of these materials during deformation. To implement this model, ABAQUS/Explicit FEA was used, which excels in simulating dynamic events such as ballistic impact. Simulations of high strain rate impact of cylindrical specimens under conditions similar to those experienced using the direct impact Split Hopkinson Pressure Bar apparatus were performed for various impact momentums over a deformation time span of 500 μs. Dynamic stress-time profiles were then computed. The results from this model were then compared to experimental results from testing performed at the University of Manitoba by others to verify the accuracy of the model.

4.2. Determination of the Johnson-Cook Plasticity Coefficients for Each Armor Material

4.2.1. Maraging Steel 300:

Maraging steels, first developed by the International Nickel Company in the 1960's, are a special class of high-strength steels that use nickel as the main alloying

element. The term “maraging” refers to “martensite age hardening” and represents the age hardening of a low-carbon, iron-nickel martensitic matrix.

Annealed maraging steel is a carbon-free, iron-nickel lath martensite. In this condition, the material is soft and can be easily machined or formed. The material is martensite at room temperature but reverts to austenitic, face-centered cubic structure when heated to 815°C. During cooling, martensite starts to form at 155°C and is 99% complete at 100°C.

For aging, the material is heated to 480°C and then cooled to room temperature. During the aging process, the martensite is strengthened by short-range ordering and subsequent precipitation of nickel-molybdenum and nickel-titanium intermetallic compounds.

Maraging steels are produced by a double-vacuum melting process to maintain high purity and to reduce residual elements. Currently only 18% nickel maraging steel alloys are produced. Higher % nickel alloys tend to be too brittle (Cubberly and Ramon 1989).

Maraging Steel 300 has a quasi-static tensile yield strength of 300 ksi (2070 MPa). Annealed maraging steel has a yield strength of approximately 110 ksi or 760 MPa. Compression values are slightly higher.

High strain rate experimental results for maraging steel at the University of Manitoba produced yield strengths of approximately 1200-1400 MPa. Yield strengths under impact are 20-30 ksi greater than those under quasi-static testing. This is consistent with the properties of annealed maraging steel 300 in compression.

The Johnson-Cook plasticity model is an empirical model deriving its constants from experimentation by using a best fit curve method of the plastic region of the stress strain curve. It uses a combination of the quasi-static results at room temperature and high strain rate results at varying rates and temperatures. This section will briefly discuss the derivation of these constants for annealed maraging steel 300 in a step-by-step manner based on the Johnson-Cook flow stress in Eq. 2-18.

4.2.1.1. Step 1: Analyzing the Quasi-static Stress Strain curve for Maraging Steel 300 in Compression:

An extensive search of published information failed to produce stress-strain relationships for annealed maraging steel 300. Only stress-strain curves for aged maraging steel were found, as shown in Figure 14.

Maraging steel 300 in compression yields at approx 1900 MPa (280 ksi) at room temperature, which is close to the yield strength of aged maraging steel 300. Benck and Silsby (1986) showed that the stress difference between the yield and ultimate strengths is no more than 70 MPa giving a very flat plastic region. Using the yield strength of annealed maraging steel 300 of 758 MPa (110 ksi) and the calculated ultimate strength, along with the elastic properties, a stress strain curve was constructed, as shown in Figure 15.

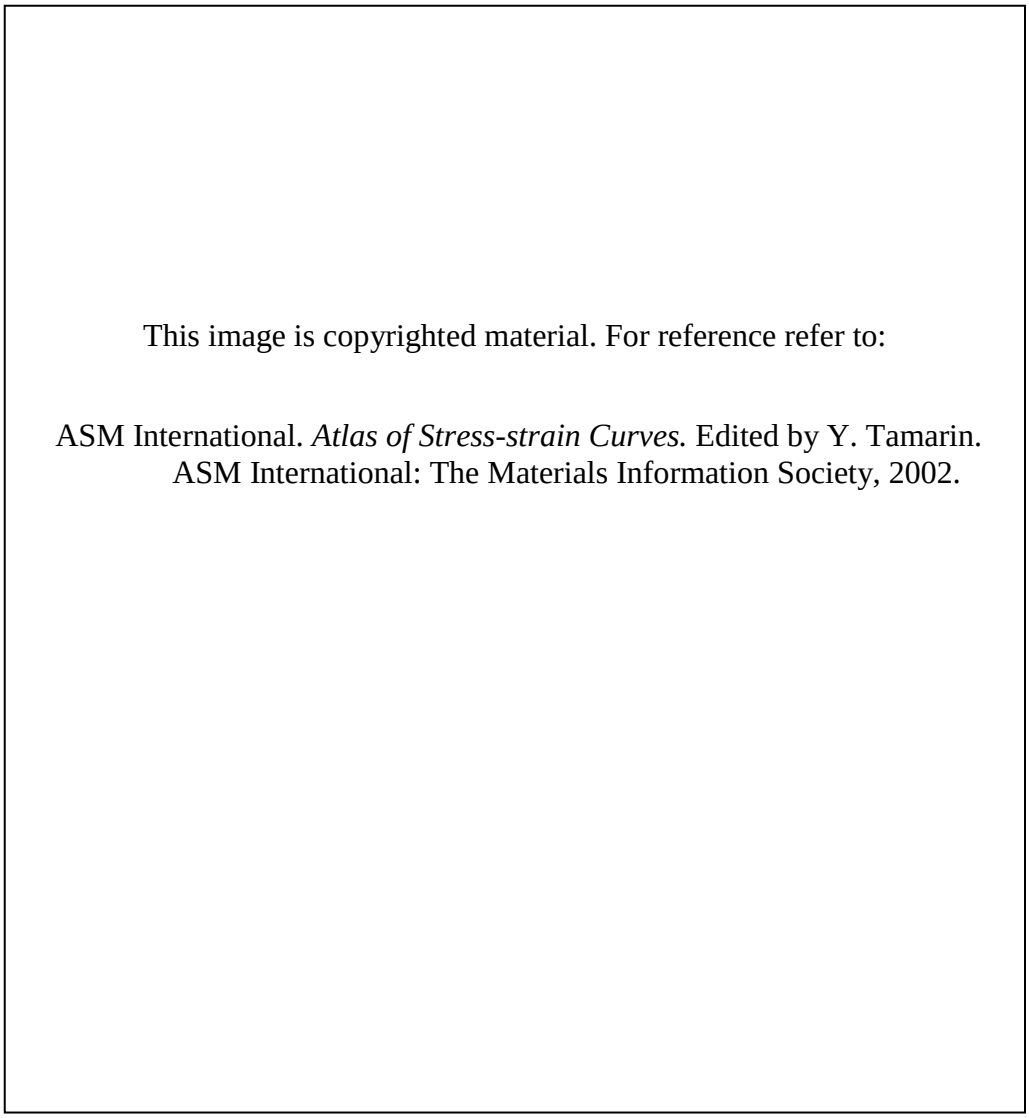

Figure 14. Quasi-static stress-strain curves for Maraging Steel 300 at various temperatures (ASM International 2002)

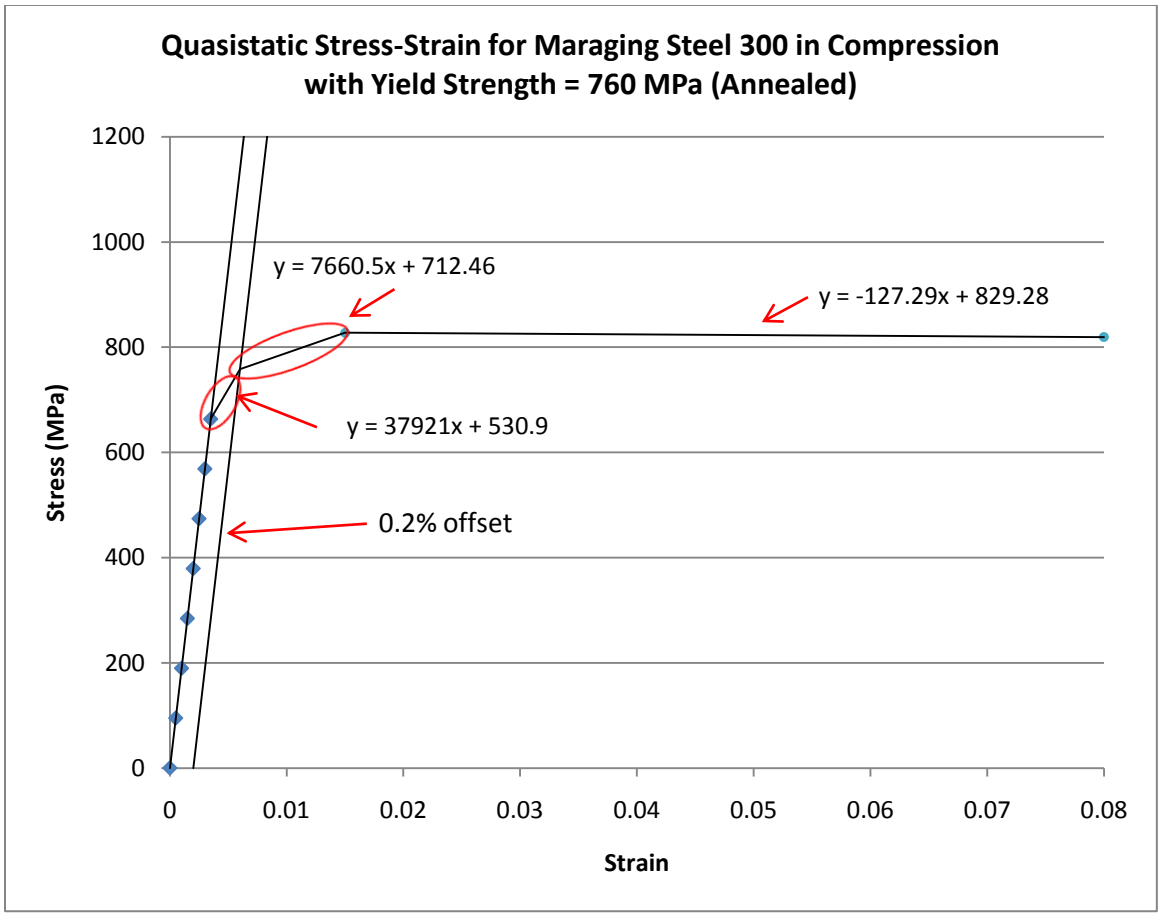

Figure 15. Constructed Stress-Strain curve for annealed Maraging Steel 300.

Any further increase in stress after the material reaches its ultimate stress would produce incorrect behavior in high strain rate compression. Thus the stress was approximated to decrease by 1% of the ultimate over 8% strain.

The first part of the Johnson-Cook equation represents the approximation to the plastic region of the quasi-static stress-strain curve. By interpolating the plot in Figure 15 using the plastic region only, the following portion of the curve shown in Figure 16 is obtained.

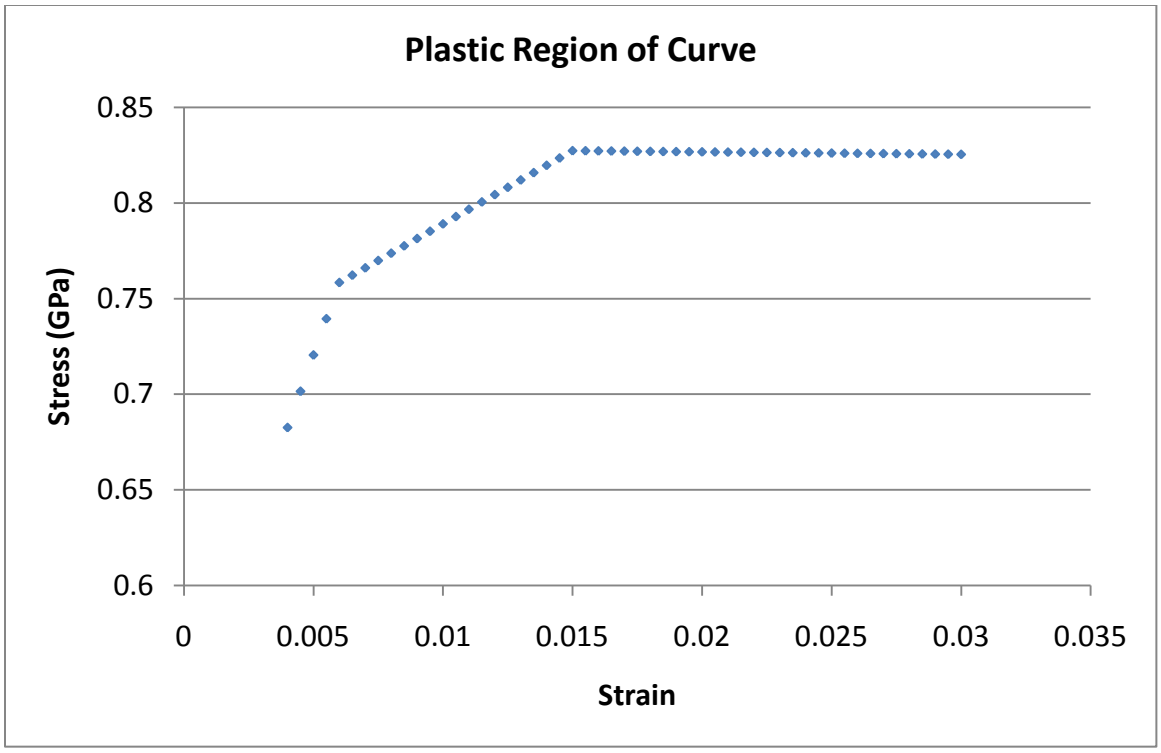

Figure 16. Plastic region of the stress-strain curve for annealed maraging steel 300

In the Johnson-Cook equation defining the isotropic hardening (Eq. 2-14), the constant 'A' represents the static yield strength, 'B' is the strain hardening coefficient, and 'n' is the strain hardening exponent. The yield strength obtained from Figure 15 is 758 MPa. Both B and n must be calculated so that this representation best fits the plastic region of the stress strain curve for maraging steel 300. In this step, only the first portion of Eq. 2-14 is considered because the temperature dependence on flow stress in negligible under quasi-static conditions.

To calculate the strain hardening factor 'B' and index 'n', a plot of Log(plastic stress) vs. Log(plastic strain) must be drawn. Both B an n must be positive to produce a

positive curvature. A linear best fit of the log-log plot of these points produces B and n, as shown in Figure 17.

The constant ‘B’ is found to be $10^{[Log(\sigma_{pl})-n*Log(\varepsilon_{pl})]}$ and constant ‘n’ is the slope of the line of best fit. If the slope is too large, an unrealistically large strain hardening takes effect during high strain rate compression and the stress rises rapidly after yield. If the slope is too small, the strain hardening effect is negligible. A negative slope gives incorrect behavior as the material will appear to weaken prematurely. In the absence of a more accurate stress-strain curve, the decision was made to select data points on the basis of assumption grounded in experimental evidence. The results are summarized in Table 1.

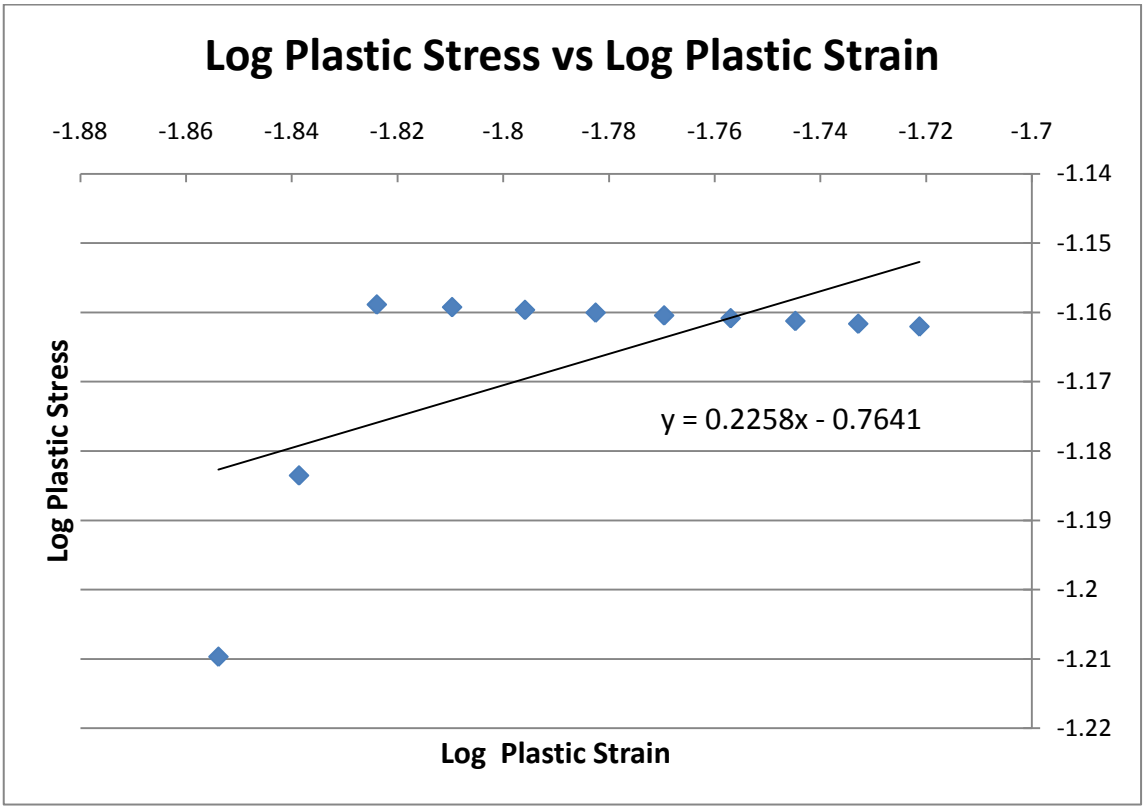

Figure 17. Log Plastic Stress vs. Log Plastic Strain for maraging steel 300

Table 1. Summary of Johnson Cook Coefficients from Quasi-static Data of Annealed Maraging Steel 300

A (GPa)	**0.758**	Yield Strength
B (GPa)	**0.172147**	$(10^{\wedge}[\text{Log}(\sigma_{pl})-n*\text{Log}(\varepsilon_{pl})])$
n	**0.2258**	(Slope of Log-Log Plot)

4.2.1.2. Step 2: Determination of the Strain Rate Sensitivity Parameter 'C':

The next step in the development of the Johnson-Cook model is to compare the plastic region of the quasi-static stress-strain curve to the newly developed Johnson-Cook approximation $\sigma = A+B\varepsilon^n$ and see where they two curves closely match. The strain value at the minimum difference between the Johnson-Cook approximated stress and the quasi-static stress in the stress-strain curve is called the static strain, which in this case is 0.0175. The corresponding (static) stress value is found to be approximately 827 MPa.

The strain rate sensitivity parameter C is found by conducting experiments at various strain rates at room temperature. In this case the experimental data from tests performed at the University of Manitoba for maraging steel 300 were used.

Six impact tests were performed for maraging steel 300 at varying strain rates, $\dot{\varepsilon}$, (Nazimuddin 2010). The stresses from experimentation at the static strain were found and are listed in Table 2.

Table 2. Summary of Dynamic Stresses gathered from experimental data for determination of the strain rate sensitivity coefficient C for Maraging Steel 300.

STATIC STRESS (GPa):	0.827052189

Determination of Strain Rate Sensitivity Coefficient [C]				
TEST #	$\dot{\varepsilon}_{avg}$ [s^{-1}]	Stress [MPa] at $\varepsilon = 0.0175$	Dynamic Stress / Static Stress	$\ln(\dot{\varepsilon})$
PRINT_00	546.134	1125.475	1.360827062	6.302864367
PRINT_01	530	1067.703759	1.290975072	6.272877007
PRINT_02	709.1625	1046.61923	1.265481482	6.564084696
PRINT_03	747.41	1135.773286	1.373278859	6.616613897
PRINT_04	928.03	1119.826128	1.353996934	6.83306406
PRINT_05	1159.029	1163.677826	1.407018616	7.055337865
PRINT_06	785.1322	1128.154853	1.364067308	6.665852111

These stresses are known as the dynamic stresses. The ratio of dynamic to static stress is greater than one, reflecting the fact that the dynamic yield stress is always greater than the static yield stress. A plot of the ratio of dynamic to static stress vs. the natural log of strain rate shows the distribution of these ratios. A line of best fit drawn from a y-intercept = 1 shows the average increase of dynamic to static stress as a function of strain rate. The slope of this line is the strain rate sensitivity parameter C, which in this case is 0.0522.

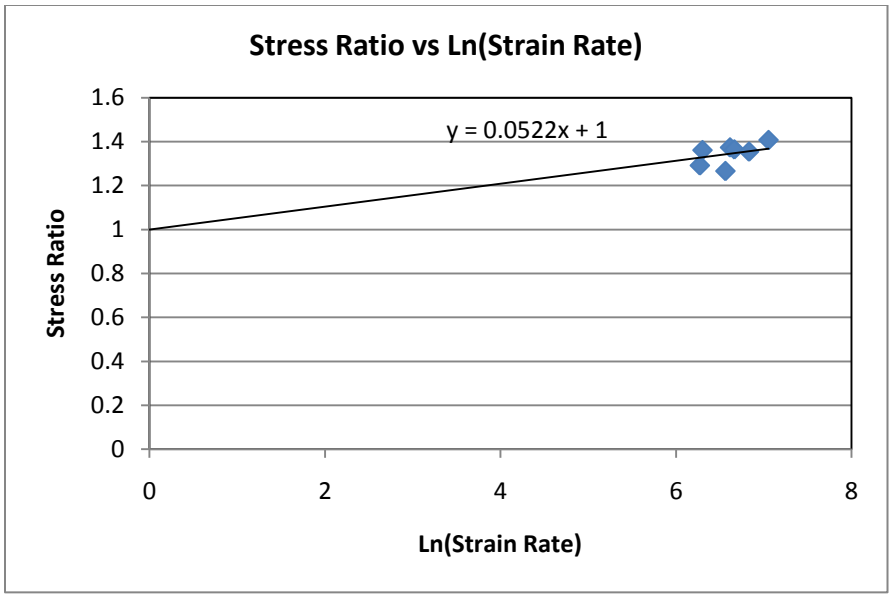

Figure 18. Dynamic to Static Stress Ratio vs. ln(Strain Rate) for Maraging Steel 300

4.2.1.3. Step 3: Determination of the Thermal Softening Coefficient 'm':

The thermal softening coefficient is taken from experiments conducted at various temperatures at a specific strain rate. This information was not available for this material. Thus a value for the thermal softening coefficient was chosen from the literature (Kennan 2005). For maraging steel 300 a thermal softening coefficient m = 0.7799 was used. A summary of the Johnson-Cook Plasticity Coefficients are shown in Table 3.

Table 3. Summary of Johnson-Cook Plasticity coefficients for Maraging Steel 300

A (GPa)	**0.758**
B (GPa)	**0.172147**
n	**0.2258**
C	**0.0522**
m	**0.7799**

4.2.2. High Hardness Armor:

High Hardness Armor (HHA) is a quenched and tempered steel armor plate suitable for use in both military and civil applications where light weight and resistance to ballistic projectiles are required. It is manufactured as a rolled steel product 8-100 mm thick that is subsequently heat treated to promote its high strength and toughness, high hardness and ballistics properties (Bisalloy Steels Australia Pty Ltd. 2008).

HHA has a typical chemical composition of 0.32 C, 0.025 P, 0.40 Mn, 0.35 Si, 0.005 S, 0.35 Ni, 1.20 Cr, 0.30 Mo, 0.002 B; with a hardness of 500 HB, a hardened yield strength of 1400 MPa and ultimate tensile strength of 1640 MPa.

The HHA specimens used in experimentation at the University of Manitoba were in their annealed softened state and had a yield strength of approximately 1200 MPa. The same procedure followed for maraging steel, as described earlier, was used to determine the coefficients for High Hardness Alloy. A summary of the results is shown in Table 4.

Table 4. Summary of Johnson-Cook Plasticity Coefficients for High Hardness Alloy

A (GPa)	**1.2**
B (GPa)	**0.300**
n	**0.8**
C	**0.003**
m	**1.17**

In this table, the thermal softening coefficient 'm' was taken from experiments performed by Gray III et al. (1994).

4.2.3. Aluminum Alloy 5083:

The 5xxx series of aluminum alloys contain magnesium, resulting in high strength and corrosion resistance. Alloys of this group are used in ship hulls and other marine applications, weld wire, and welded storage vessels. The strength of alloys in this series is directly proportional to the magnesium content, which ranges up to about 6% (Wessel 2004).

Aluminum alloy 5083 (AA5083) is a moderate strength alloy with very good corrosion resistance. It has high weldability and is used in transportation, pressure vessels, cryogenics, towers and drilling rigs, gas/oil piping, ordinance, and armor plating. Its chemical composition is made up of 0.25 Cu, 0.1 Fe, 0.4 Mg, 4.9 Mn, 0.4 Si, 0.15 Ti, 0.25 Zn.

Aluminum alloy 5083 is a non heat-treatable alloy which is typically annealed at approximately 345°C for sufficient time and then air cooled. Hardening is accomplished by means of cold working only. Annealed Aluminum alloy 5083 is designated by "-O". Aluminum alloy 5083-H131 (MIL-DTL-46027) is a non-heat-treatable, strain-hardened aluminum magnesium alloy, resistant to cracking and stress-corrosion cracking. It can be readily weldable and has excellent corrosion resistance. The M113 Armored Personnel Carrier, M109 Paladin Self Propelled Howitzer and the lower half of the Bradley Fighting Vehicle are made from AA5083 (The United States Department of Defense 2004). AA5083-O/-H131 both have similar quasi-static mechanical properties with a compression yield strength of approximately 145 MPa (The Aluminum Association Inc. 2009).

Other than having a lower yield strength (0.2% offset) than steel, aluminum alloys are softer and more ductile than steels. In quasi-static deformation aluminum alloys have a large plastic region (larger zone of strain hardening up to ultimate stress). Under quasi-static conditions ($<10^{-3}$ /s strain rates) the stress strain behavior of AA5083-H131 in tension and compression are almost identical, apart from having different elastic moduli. A typical stress strain curve for AA5083-O in tension obtained by normalized test ASTM E 8M-89 in an 8033 Instron machine by Canas et al. (1994) is shown in Figure 19.

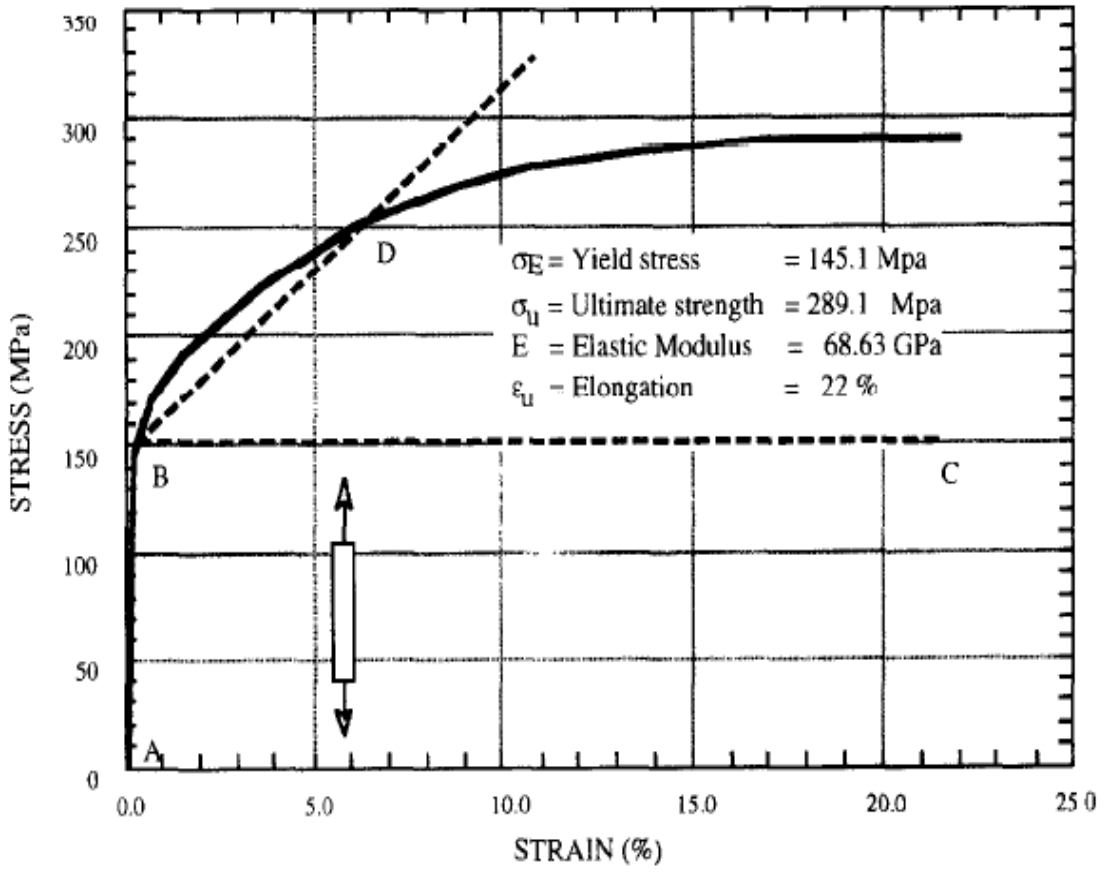

Figure 19. Quasi-static Tensile Stress Strain Curve for Aluminum Alloy 5083-O

Following the same procedure as the one used for the other two metals the best Johnson-Cook approximation to the plastic stress-strain curve is shown in Figure 20.

The graph in Figure 20 is derived from the definition of flow stress based on the Johnson-Cook Hardening Law (Eq. 2-14) where A is the quasi-static yield strength and B and n are the strain hardening components. The Johnson-Cook coefficients for AA5083-H131 are summarized in Table 5.

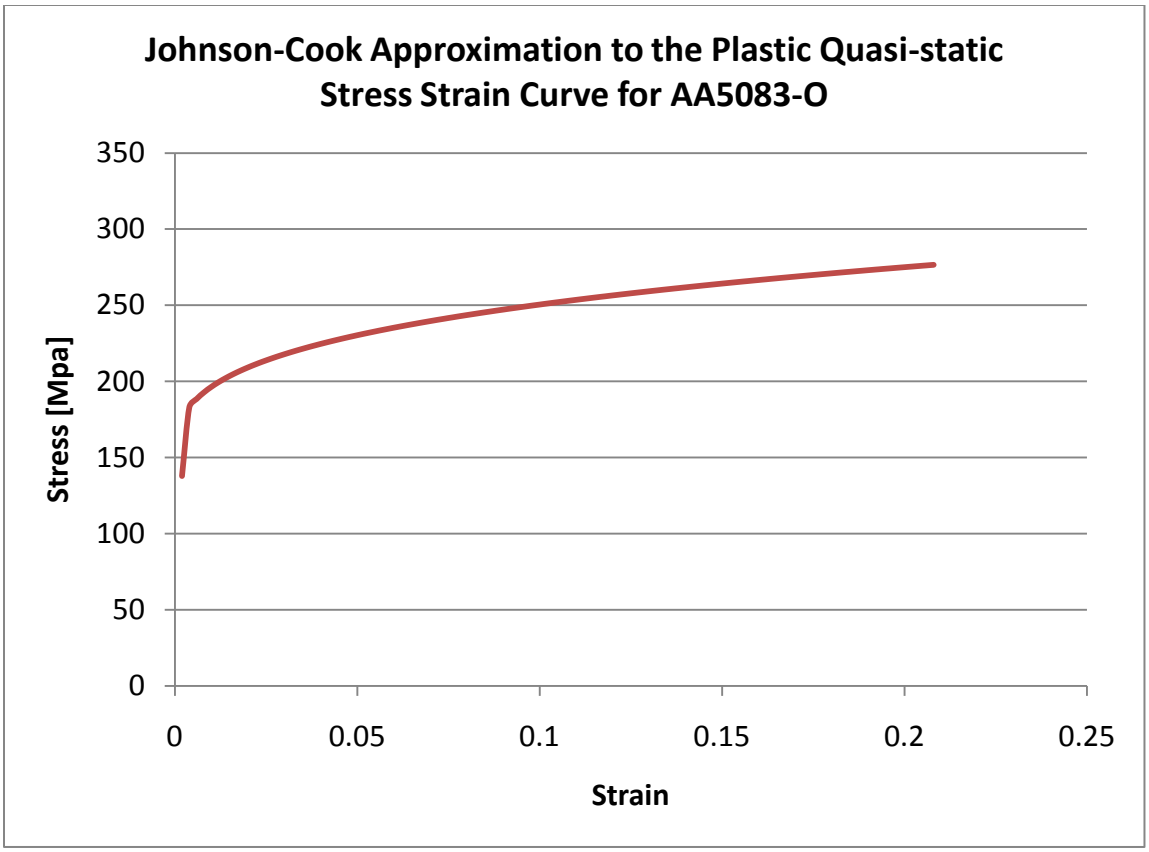

Figure 20. Johnson-Cook Approximation to the Plastic QS Stress-Strain Curve for AA5083-O

Table 5. Summary of Johnson-Cook Plasticity Coefficients for Aluminum Alloy 5083

A (GPa)	**0.13789**
B (GPa)	**0.21673**
n	**0.4845**
C	**0.002**
m	**1.225**

As in the previous cases, the thermal softening coefficient 'm' was taken from experiments performed by Gray III et al. (1994).

4.3. Finite Element Software Package ABAQUS 6.8

ABAQUS is a finite element analysis tool used by engineers and material scientists to model the predictive behavior of materials and structures. It can be used to solve problems ranging from simple linear analyses to advanced nonlinear simulations, including problems that involve static, dynamic, thermal, and electrical response of components (ABAQUS Users' Manual 2008). ABAQUS is used in aeronautics and automotive engineering because it excels in simulating explicit dynamic time-dependent problems, such as blast, impact, and fracture mechanics applications.

4.4. Implementation of Material Parameters into ABAQUS

For each of the metals, whose behavior was examined in the current investigation, a separate material library was constructed. Along with implementing the Johnson-Cook material models which define how the materials behave plastically, physical and thermal properties, such as density, coefficient of thermal expansion, heat fraction, and specific heat capacity were also incorporated to describe the effects of heating caused by high strain rate deformation on the mechanical behavior of the material. A simple isotropic elastic model using ASTM data for each material in compression was included to describe the elastic behavior of the materials.

Due to the limited data for the specific mechanical properties of the materials examined in this thesis, information for calculating the failure parameters required by the Johnson-Cook Dynamic Failure Model was based on metals whose physical properties

were in close agreement to the armor metals used in this thesis. A summary of the input parameters for each of the metals examined is given in Tables 6 through 8.

MARAGING STEEL 300:

Table 6. Summary of material parameters for Maraging Steel 300

Category	Parameter Name	Value	Source
Physical Properties	Density	7999.49246 kg/m^3	(ATI Properties Inc. 2000)(United States of America Department of Defense 1998)
Thermal Properties	Thermal Conductivity	19.6 W/(m.K)	
	Coefficient of Thermal Expansion	9 x 10^{-6} /K	
	Inelastic Heat Fraction	0.9	
	Specific Heat Capacity	452 J/(kg.K)	
Isotropic Elastic Model	Young's Modulus	192 GPa	
	Poisson's Ratio	0.283	
Johnson Cook Plasticity Model	A	758.423 MPa	Calculated from experimentation at the University of Manitoba
	B	172.147 MPa	
	n	0.2258	
	C	0.0522	
	m	0.7799	
	T_m	1685 K	(ATI Properties Inc. 2000)
	T_{ref}	293 K	
Johnson Cook Dynamic Failure Model	d1	-0.09	Failure parameters for Ti-6Al-4V whose physical properties are close that of annealed maraging steel 300 (EIToby, Ng and Elbestawi 2004)
	d2	0.27	
	d3	0.48	
	d4	0.014	
	d5	3.870	
Damage Evolution	Fracture Energy	14.4 J	Average value for 18Ni(350) Maraging Steel annealed at 815^{o}C. (Kalish and Rack 1971)

HIGH HARDNESS ARMOR:

Table 7. Summary of material parameters for High Hardness Armor

Category	Parameter Name	Value	Source
Physical Properties	Density	7860 kg/m^3	(United States of America Department of Defense 1998) (Bisalloy Steels Australia Pty Ltd. 2008)
Thermal Properties	Thermal Conductivity	20 W/(m.K)	
	Coefficient of Thermal Expansion	9 x 10^{-6} /K	
	Inelastic Heat Fraction	0.9	
	Specific Heat Capacity	452 J/(kg.K)	
Isotropic Elastic Model	Young's Modulus	205 GPa	
	Poisson's Ratio	0.293	
Johnson Cook Plasticity Model	A	1200 MPa	Calculated from experimentation at the University of Manitoba
	B	300 MPa	
	n	0.8	
	C	0.003	
	m	1.17	
	T_m	1783 K	(Bisalloy Steels Australia Pty Ltd. 2008)
	T_{ref}	293 K	
Johnson Cook Dynamic Failure Model	d1	0.1	Failure parameters for HHA-2P whose physical properties are close that of annealed HHA used in this thesis (Buchar, et al. 2002)
	d2	0.93	
	d3	-1.08	
	d4	0.000014	
	d5	0.65	
Damage Evolution	Fracture Energy	35 J	(Bisalloy Steels Australia Pty Ltd. 2008)

ALUMINUM ALLOY 5083-H131:

Table 8. Summary of material parameters for Aluminum Alloy 5083-H131

Category	Parameter Name	Value	Source
Physical Properties	Density	2660 kg/m^3	(United States of America Department of Defense 1998)
Thermal Properties	Thermal Conductivity	120 W/(m.K)	
	Coefficient of Thermal Expansion	2.34x10^{-7} /K	
	Inelastic Heat Fraction	0.9	
	Specific Heat Capacity	900 J/(kg.K)	
Isotropic Elastic Model	Young's Modulus	71.7 GPa	
	Poisson's Ratio	0.33	
Johnson Cook Plasticity Model	A	137.89 MPa	Calculated from experimentation at the University of Manitoba
	B	216.73 MPa	
	n	0.4845	
	C	0.002	
	m	1.225	
	T_m	933 K	(United States of America Department of Defense 1998)
	T_{ref}	293 K	
Johnson Cook Dynamic Failure Model	d1	0.178	Failure parameters for AA5083-H116 (Grytten, et al. 2007)
	d2	0.389	
	d3	-2.246	
	d4	0	
	d5	0	

4.5. Modeling the modified Split Hopkinson Bar Apparatus in ABAQUS

4.5.1. Design:

To properly simulate the conditions for high strain rate compression, a simplified split Hopkinson bar apparatus was modeled into ABAQUS. The model consisted of three parts: the projectile, transmitting bar and the test specimen. The projectile and transmitting bars were modeled as simple cylinders whose diameters were 3.8 cm. The schematics used in the model are shown in Figure 21.

Both transmission and projectile bars were assigned the material properties of AISI 4340 steel using a simple elastic model. Their existence was necessary to properly simulate the impact forces and conditions under which the test specimen was subject to during testing.

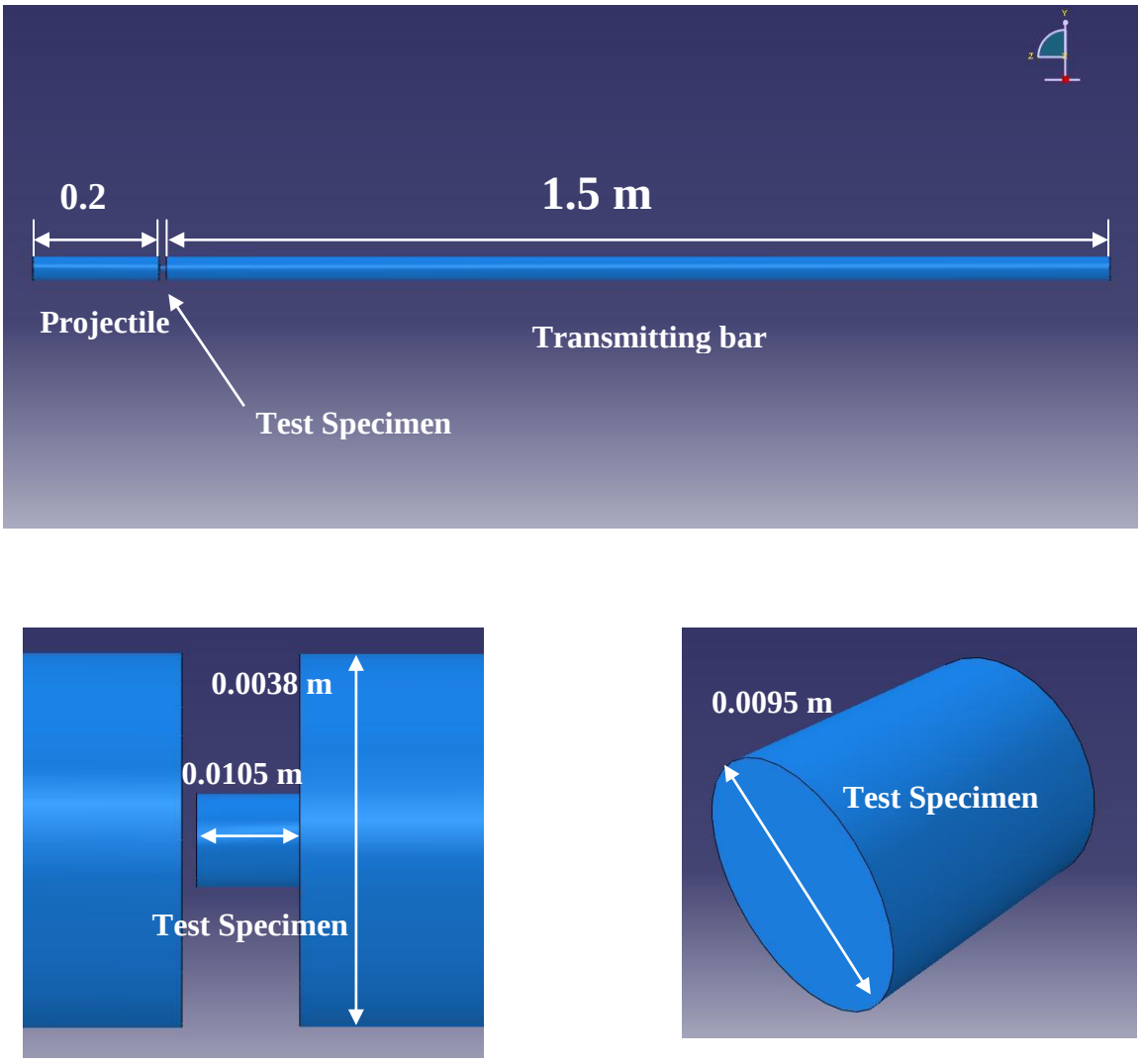

Figure 21. Schematics of modeled apparatus in ABAQUS

The student version of ABAQUS limits the number of allowable nodes to 1000. Since information from either the projectile or the transmission bar was not as important as that of the test specimen, they were assigned a very course mesh. The test specimen, however, was modeled using an 8-node hex element mesh using 488 elements as seen in Figure 22. This is the finest mesh available for this version of the FEM program.

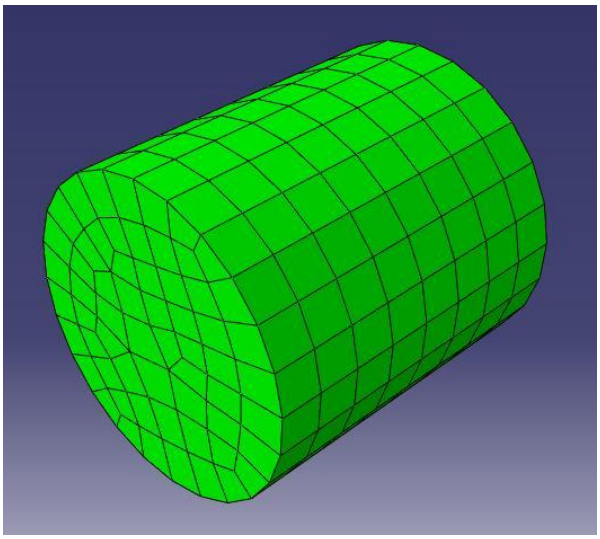

Figure 22. Isometric view of meshed specimen

To minimize computation time, the modeled projectile was positioned very close to the test specimen. In experiments, the projectile is housed in a tube and fired from a position approximately two meters away from the test specimen. The modified split Hopkinson Bar apparatus used at the University of Manitoba was set up so that the projectile would be fired at specific firing pressures measured by the amount of pressure built up in the compressed air firing chamber. In her thesis, Mirfakhraei (2008) measured the corresponding impact velocities for the various firing pressures. The averages were

calculated and are shown in Table 9. These velocities were used as initial conditions for the projectile in the model.

Table 9. Input parameters for ABAQUS

Firing Pressure [kPa]	Impact Velocity [m/s]	Impact Momentum [kg.m/s]
400	34.88	62.10
360	33.32	59.32
340	32.18	57.31
320	31.35	55.84
280	29.12	51.86
240	26.93	47.96
220	25.82	45.97
200	25.17	44.83
180	24.13	42.97
150	22.53	40.12
140	21.08	37.53
120	19.13	34.06
100	18.32	30.85
80	13.98	24.91
60	11.42	20.34

Firing the projectile at various velocities would produce dynamic stress responses showing the deformation behavior of the test specimen under varying impact momentums. To this end calculations were performed for increasing firing speeds for the purpose of creating a deformation map showing the changes in the behavior of specimens over time and then comparing to experimental results to ensure accuracy.

The parameters summarized in this chapter for each of the armor materials, developed from experimental data, were used to create material databases. Given their versatility, these databases can be used to simulate deformation at high strain rate in any direction including both tension and torsion as well as in compression. High strain rate compression simulations were chosen since experimental data were readily available for specimens tested under these conditions. In each simulation, the compressive stress in each element of the specimen mesh was computed and the maximum overall stress was determined and plotted vs time. A review of the dynamic stress responses for each of the armor materials is given in the following sections.

5. RESULTS AND DISCUSSION

Calculations were performed for a range of different impact momentums reflecting experimental tests carried out at the University of Manitoba. Impact momentum was chosen as opposed to impact velocity as a way to normalize the initial conditions for each test. To this end, the stress responses of the specimens were independent of the properties of the projectile used during simulation. Maximum compressive stress-time curves were generated for impact momentums ranging from 14 kg.m/s to 52 kg.m/s for maraging steel 300 and high hardness armor (HHA) and 25 kg.m/s to 40 kg.m/s for aluminum alloy 5083-H131.

5.1. Shear Failure Analysis

From computational results (Figures 23 to 25), it was found that the first occurrence of shear failure nucleates at the center of the specimen during high strain rate compression. Taking a longitudinal cross section of the specimen, as shown in Figure 25, it is seen that at certain impact momentums indicative of shear band formation, shear failure at propagates from the center of the specimen diagonally to the corners. This occurs in both BCC metals (MS300 and High Hardness Armor). This is reflected in Figure 23, showing a plot of shear stress vs. time for maraging steel 300 at a specific impact momentum that induces shear failure. Each curve represents the maximum shear

stress over time in an element located along the cross-sectional diagonal as a function of distance from the edge of the specimen (shown in Figure 25 as a percent of the total length).

From Figure 23, it appears that the shear failure propagates in opposite directions at different speeds. This is partly due to the course discretization of the mesh used for the specimen model. By increasing the number of elements in the mesh, a more accurate picture of the progression of shear failure would be evident. This analysis is only to show the concept of progressive shear failure in the elements from the center to the outer edges.

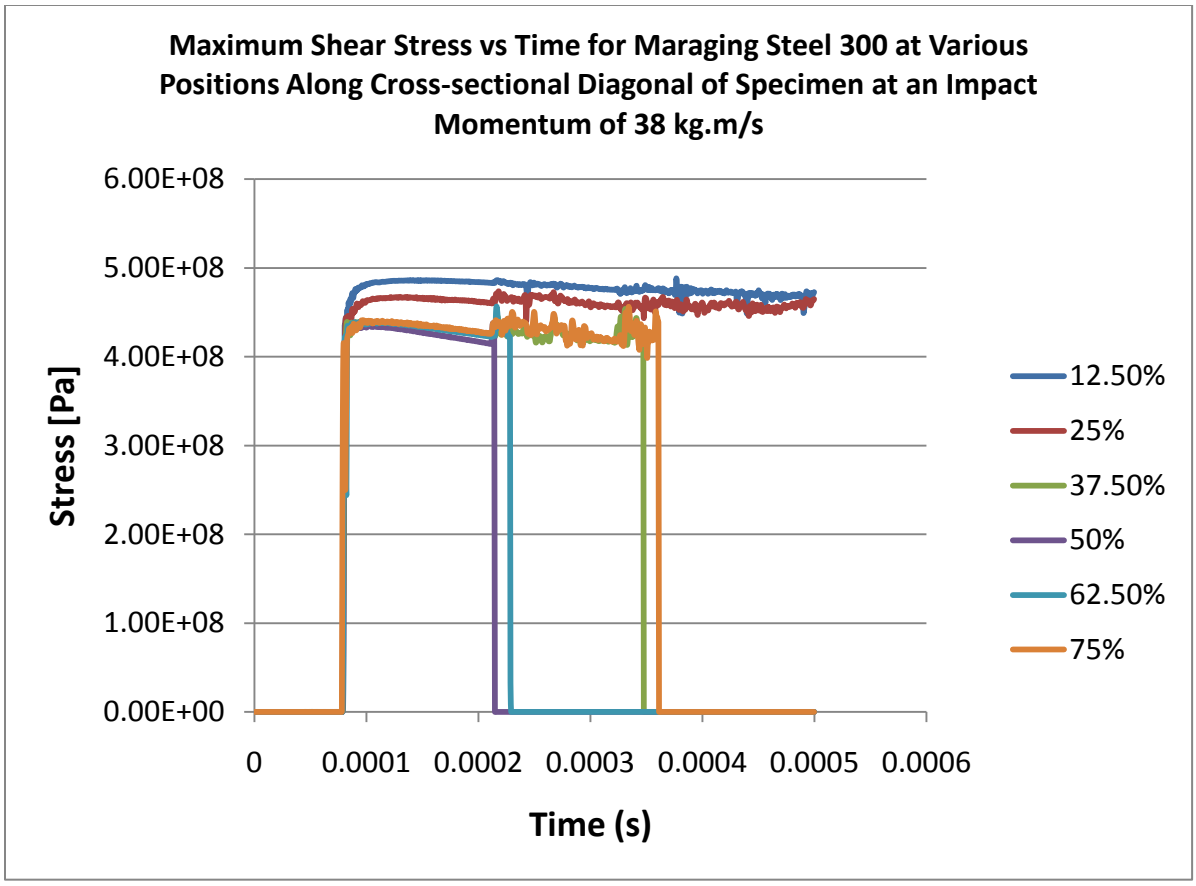

Figure 23. Maximum shear stress as a function of time for maraging steel 300

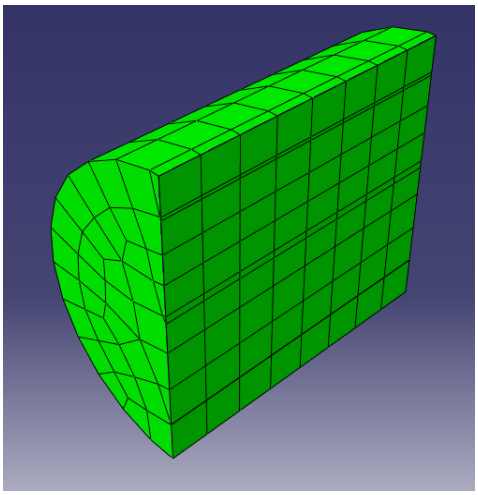

Figure 24. Isometric cross section of test specimen

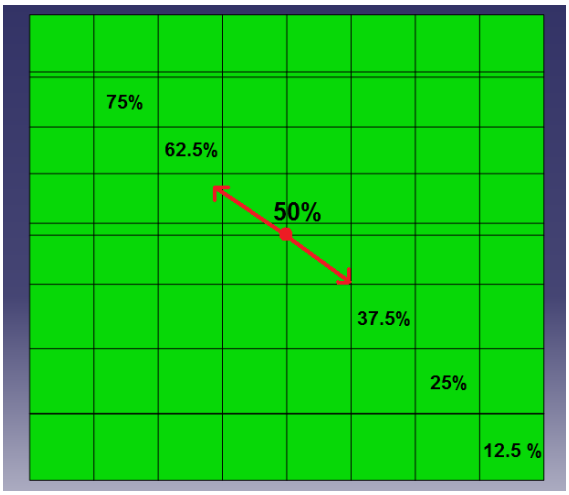

Figure 25. Nucleation and propagation of shear failure as a function of distance from the edge (given in % of the total length of the specimen)

Looking at the cross section of the specimen in Figure 25, this seemingly straight line of shear failure becomes “S” shaped when the specimen is fully deformed. In 3D the shear failure is in the shape of an hourglass, as shown in Figure 26.

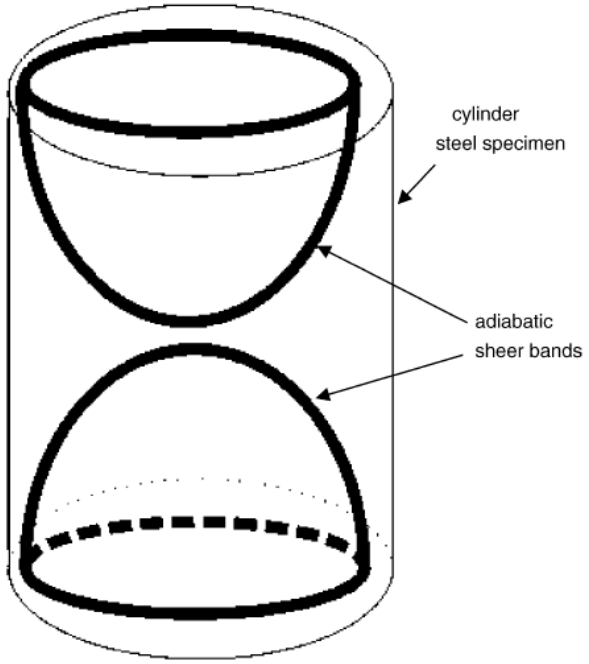

Figure 26. Schematic representation of a 3D view of the adiabatic shear bands formed in cylindrical steel specimens (A. Odeshi, M. Bassim, et al. 2005)

A visual representation of the progression of shear failure in a specimen made from maraging steel 300 over a time of 0.5ms—subjected to an impact momentum of 38 kg.m/s is shown in Figure 27. Areas shown in blue represent complete shear failure. Similar results are shown in Figures 28 and 29 from experimentation conducted under conditions of high strain rate compression of specimens of comparable geometry. The hourglass formation of shear failure is evident in both results, even showing the formation of adiabatic shear bands along these lines of shear failure.

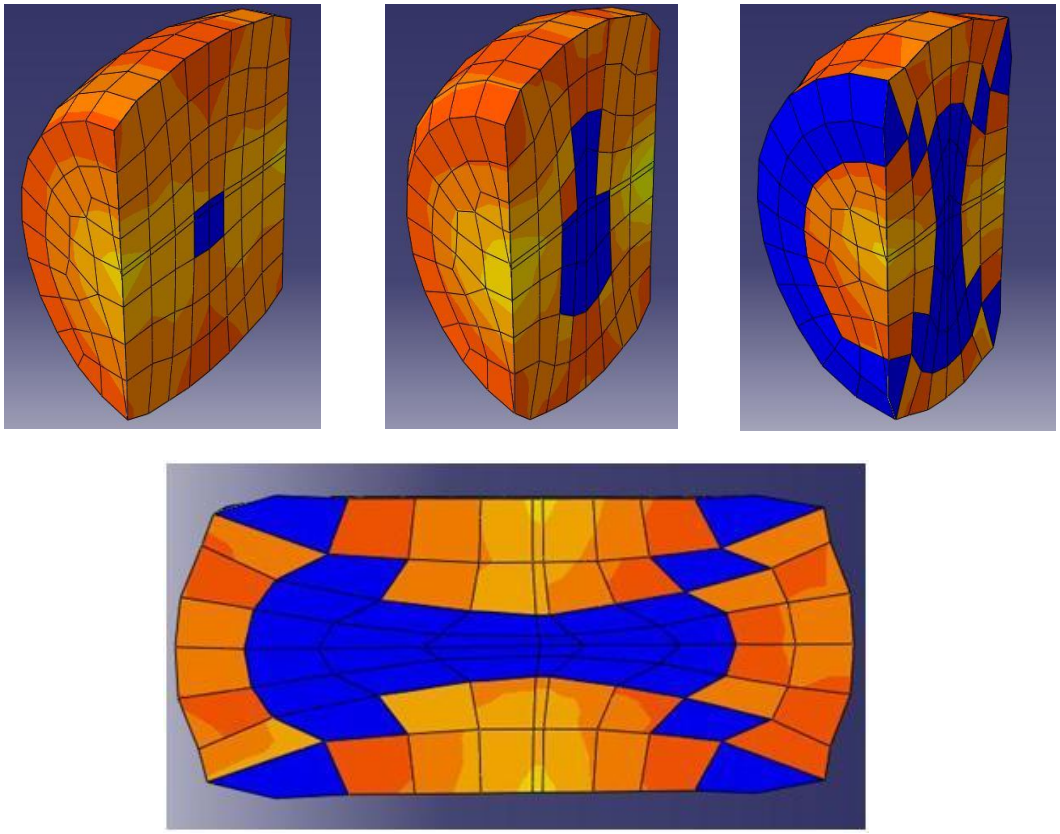

Figure 27. Cross-sectional shear failure of a maraging steel 300 specimen subject to an impact momentum of 38 kg.m/s

Figure 28. Cross-section of Ti-15Mo-5Zr-3Al specimen deformed at 8×10^{-3} /s (Lee, Lin, et al. 2008)

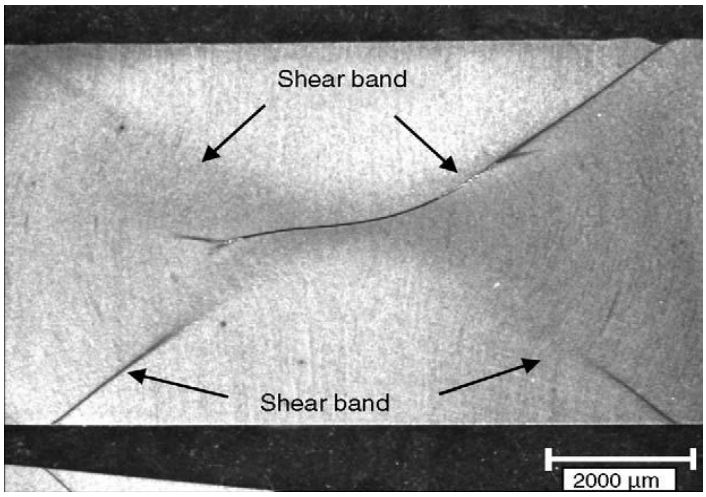

Figure 29. Photomicrograph of a longitudinal section of an impacted specimen of AISI 4340 Steel (A. Odeshi, M. Bassim, et al. 2005)

For each of the materials modeled, the shear stress in the center of the specimen was used to indicate the first occurrence of shear failure during compression. It was used, along with the maximum compressive stress responses, in order to clearly identify the time at which the compressive stress reaches a maximum and the subsequent effect on the mechanical behavior of the material—linking it to the possibility of the formation of adiabatic shear bands. These results were compared with experimental stress-time histories and are discussed in the next section.

5.2. Stress-time Results for Maraging Steel 300

Stress-time plots for maraging steel 300 for a range of impact momentums were compiled to show the changing characteristics of the metal under varying loading conditions and the nucleation and localization of shear failure. The maximum compressive stress in the specimen along with the maximum shear stress in the center of the specimen, were considered. A series of stress-time plots for selected momentums are given in Figures 30 through 32. Results gathered from experiments conducted at the University of Manitoba are used to compare and gauge the accuracy and validity of the theoretical values.

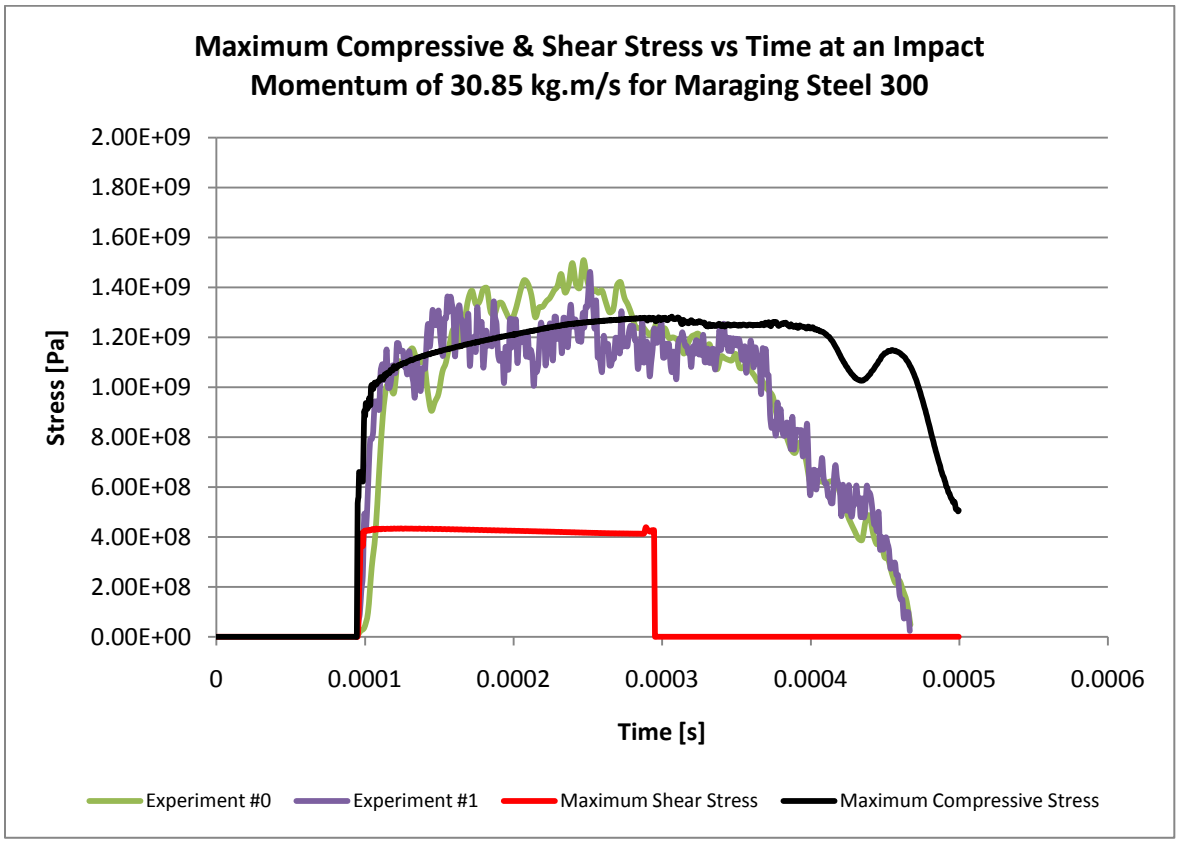

Figure 30. Stress-time history of MS300 at an impact momentum of 30.85 kg.m/s (Experimental results from Nazimuddin (2010))

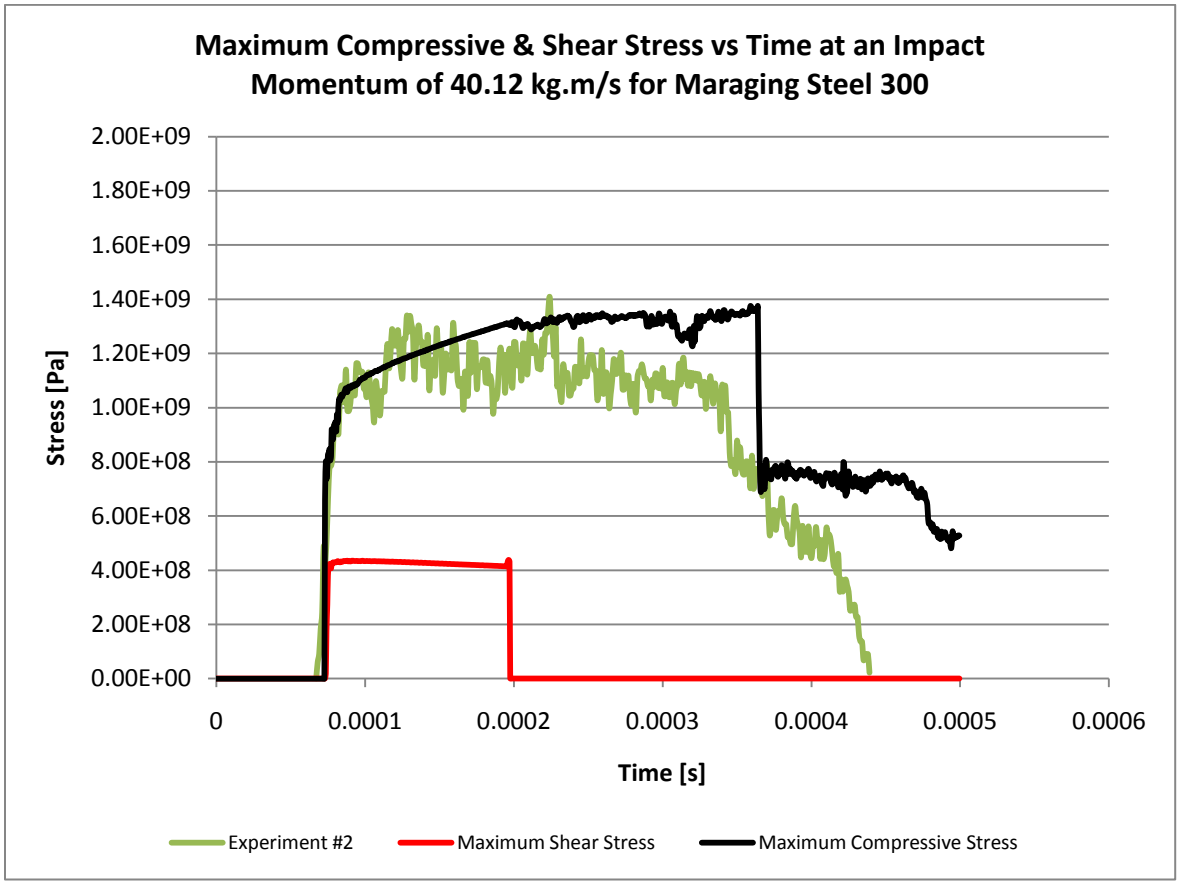

Figure 31. Stress-time history of MS300 at an impact momentum of 40.12 kg.m/s (Experimental results from Nazimuddin (2010))

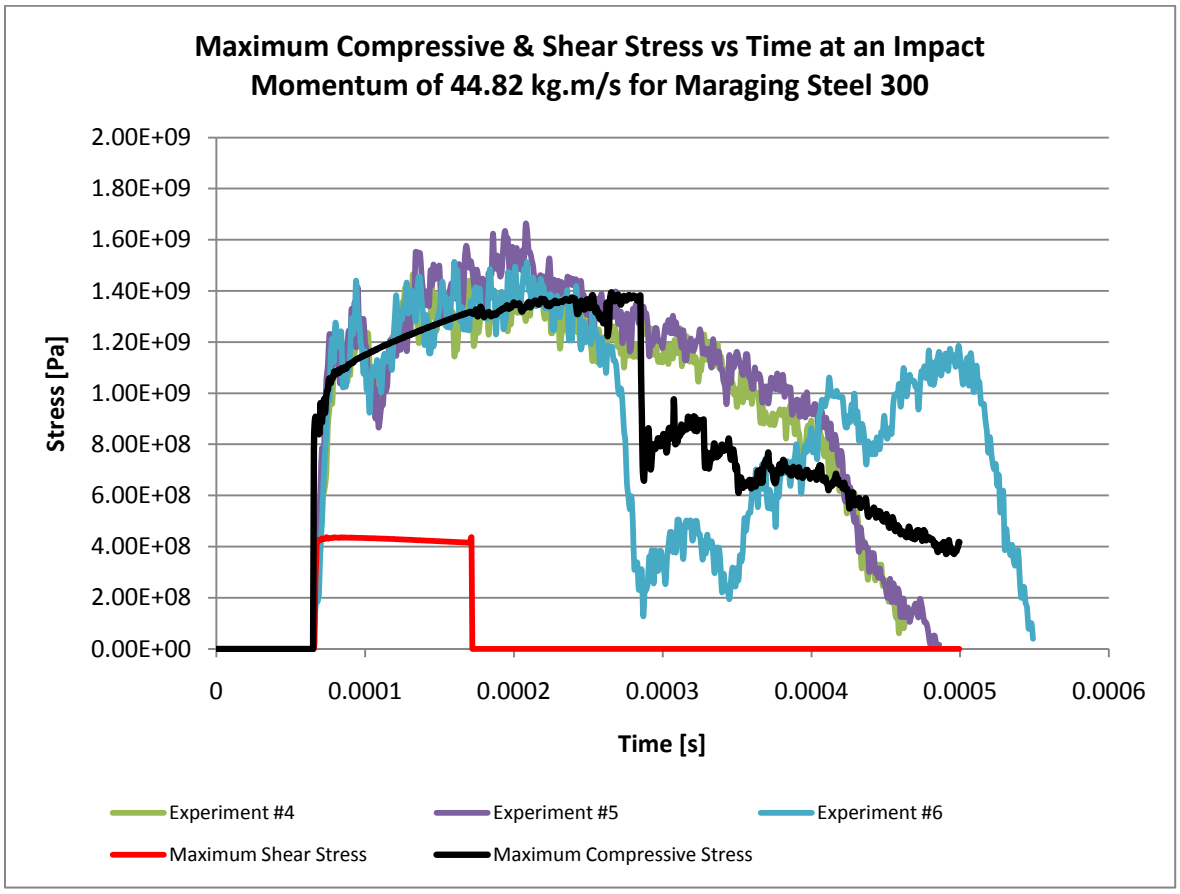

Figure 32. Stress-time history of MS300 at an impact momentum of 44.82 kg.m/s (Experimental results from Nazimuddin (2010))

It is evident that the Johnson-Cook model was successfully used to simulate the behavior of the tested maraging steel 300 specimens. It is also interesting to note that upon shear stress failure in the center of the specimen, there begins an instability in maximum compressive stress capacity which is further degraded by the consecutive shear failures of adjacent elements in the model. Experimental results show a drop in stress capacity at the first occurrence of the computed shear failure, after which the specimen undergoes thermal softening and finally ultimate failure. The subsequent large drops in stress capacity are attributed to fracturing of the specimen, as reflected in one of tested specimens.

As it stands, the Johnson-Cook model does not properly show the effects of thermal softening. One explanation could be that the strain rate sensitivity, temperature, and strain are independent of one another in the constitutive equations. In reality this is not the case. The temperature rise in metals that occurs during high strain rate deformation leads to an instability which dynamically alters the mechanical properties of the material, often changing the microstructure. Thus, at the point of thermal instability, where softening occurs, temperature, strain, and strain rate become dependent on each other and the properties of the material change. However, in the Johnson Cook model, these properties remain constant, and the material is treated as homogeneous with no microstructural changes. The temperature effect on the flow stress in the model only serves to scale the overall dynamic stress behavior up and down depending on the initial temperature and melting point of the specimen.

The time of shear failure at the center of the specimen obtained from computations closely matches the time at which the maximum stress is reached in the experimentation. While the stress collapse in the experimental data is due to a combination of mechanical and thermal instabilities (i.e. thermal softening or possible nucleation of adiabatic shear bands), the stress collapse from modeled results is caused by the initiation and propagation of shear failure in consecutive elements—a purely mechanical instability.

In the stress-time plot for an impact momentum of 44.82 kg.m/s, shown in Figure 32, fracture was observed in both the theoretical model and in one of the specimens tested. However, at an impact momentum of 40.12 kg.m/s, shown in Figure 31, fracture was observed in the model but not in the tested specimen. One explanation may be tied to the fact that the Johnson-Cook constitutive model does not show the effects of thermal softening. As mentioned previously, the temperature component in the Johnson-Cook model is only used to scale the stress behavior of the material as a whole. Microstructural changes caused by thermal instabilities are not considered and shearing occurs solely due to mechanical instabilities during deformation, defined by the failure parameters in the Johnson Cook dynamic failure model. To this end, the modelled specimen will indicate fracture at lower strain rates compared to that in the experimentation.

It is important to note that the Johnson-Cook model is strictly phenomenological, defining the mechanical behavior of materials using power law hardening and scaling it up and down depending on the strain rate and temperature (Thomson 2006). The Johnson Cook model does not properly account for materials where the effect of strain rate and

temperature on the flow stress is dependent on strain; like that for FCC metals (Gray III, et al. 1994, Zerilli and Armstrong 1987). This will be discussed in more detail in Section 5.4.

5.3. Stress-time Results for High Hardness Armor

The deformation of high hardness armor is similar to that of maraging steel. The stress-time plots for two different impact momentums for high hardness armor are shown in Figures 33 and 34.

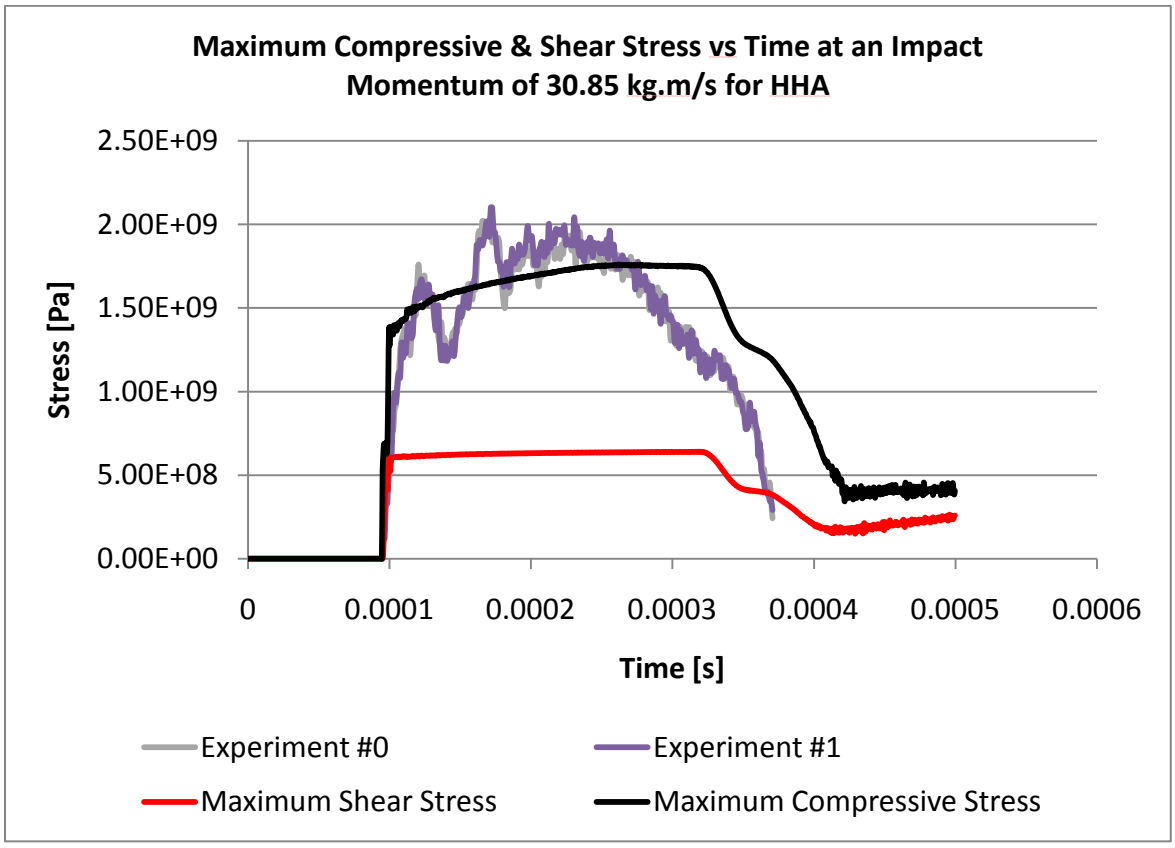

Figure 33. Stress-time history of high hardness armor at an impact momentum of 30.85 kg.m/s (Experimental results from Nazimuddin (2010))

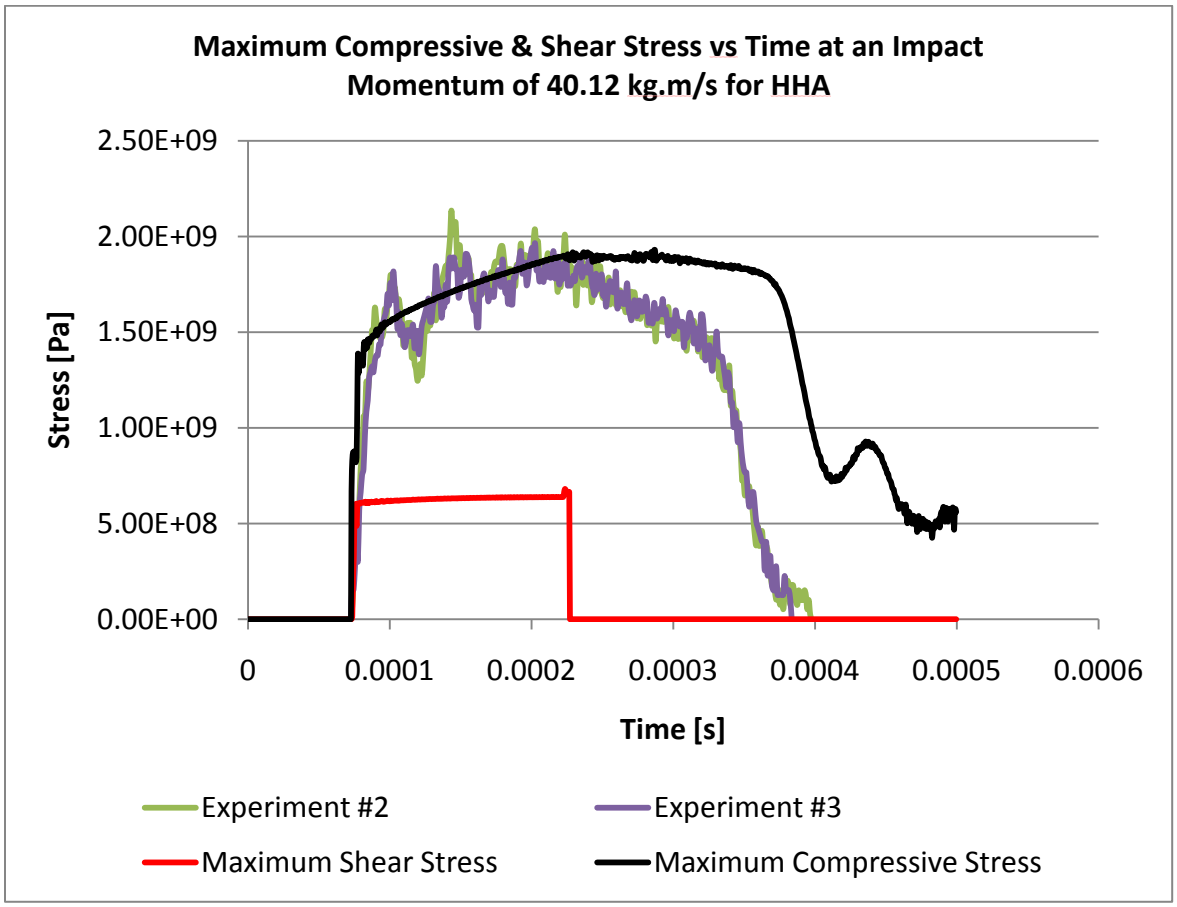

Figure 34. Stress-time history of high hardness armor at an impact momentum of 40.12 kg.m/s (Experimental results from Nazimuddin (2010))

The modeled results at the lower momentum of 30.85 kg.m/s, shown in Figure 33, show no shear failure nucleation in the specimen. However, the maximum computed compressive stress occurs at a time close to that observed in the experimental results. Although a reduction in the computed compressive stress is observed, the computed shear stress shows no visible changes or instabilities. The sudden drop in the computed compressive stress, after reaching a maximum, is due to the release of the applied load.

At an impact momentum of 40.12 kg.m/s, shown in Figure 34, the behavior of high hardness armor (HHA), simulated by the Johnson-Cook model, is similar to that of maraging steel 300 whereby shear failure in the material causes an instability in the maximum compressive stress that takes place at a time that coincides with the peak compressive stress reached in experimental results.

It is known that transformed bands in BCC metals can lead to complete shear failure, caused by a hardening and subsequent brittle failure along the band to the edges of the material. Deformed bands also lead to loss in stress capacity in the material, both in compression and in shear. In the modeled results for maraging steel 300, the minimum impact momentum for complete shear failure was at 38 kg.m/s, whereby shear failure propagated through the length of the specimen, as indicated in Figure 27. According to experimental observations, transformed shear bands were first observed in maraging steel 300 specimens impacted at 44.83 kg.m/s (Nazimuddin 2010). Both modeled results and experimental observations are in close agreement.

For high hardness armor, shear failure first occurred in the model between impact momentums of 37.85-40.12 kg.m/s. Experimental observations showed that faint

deformed bands appeared in specimens subjected to an impact momentum just below this range at 30.85 kg.m/s, gradually becoming more clear and defined for impact momentums at 40.12 kg.m/s and 44.83 kg.m/s (Nazimuddin 2010). It can be concluded that, while accurate to some degree, the model is rather insensitive to the minute physical and microstructural changes in the metal, only reflecting large instabilities during deformation. Refining the discretization of the elements with a finer mesh could improve the accuracy of the results.

It cannot be discerned from the modelled stress-time plots whether or not the failure is due to shear band formation. The shear failure that occurs in the center of the specimen may not propagate to the edges, which is indicative of complete shear failure for all impact momentums. It is, however, used as a marker to show when the maximum compressive stress is reached. Only by visual observation of the shear propagation in the model, during compression, can it be concluded that there is complete shear failure. The microstructural changes that the material undergoes during shear band formation, such as rearrangement and rotation of grains and even phase changes are not taken into account. The Johnson-Cook model is empirical and not physical-based and is only as accurate as the experimental results and the finite element code.

5.4. Stress-time results for aluminum alloy 5083-H131

As mentioned earlier, the Johnson-Cook model does not accurately depict the behavior of FCC materials, such as aluminum alloys and copper. This was evident in the results from stress-time plots for AA5083-H131 at various increasing impact momentums. The theoretical results are shown in Figures 35 through 37. Experimental results are also included in these figures for comparison.

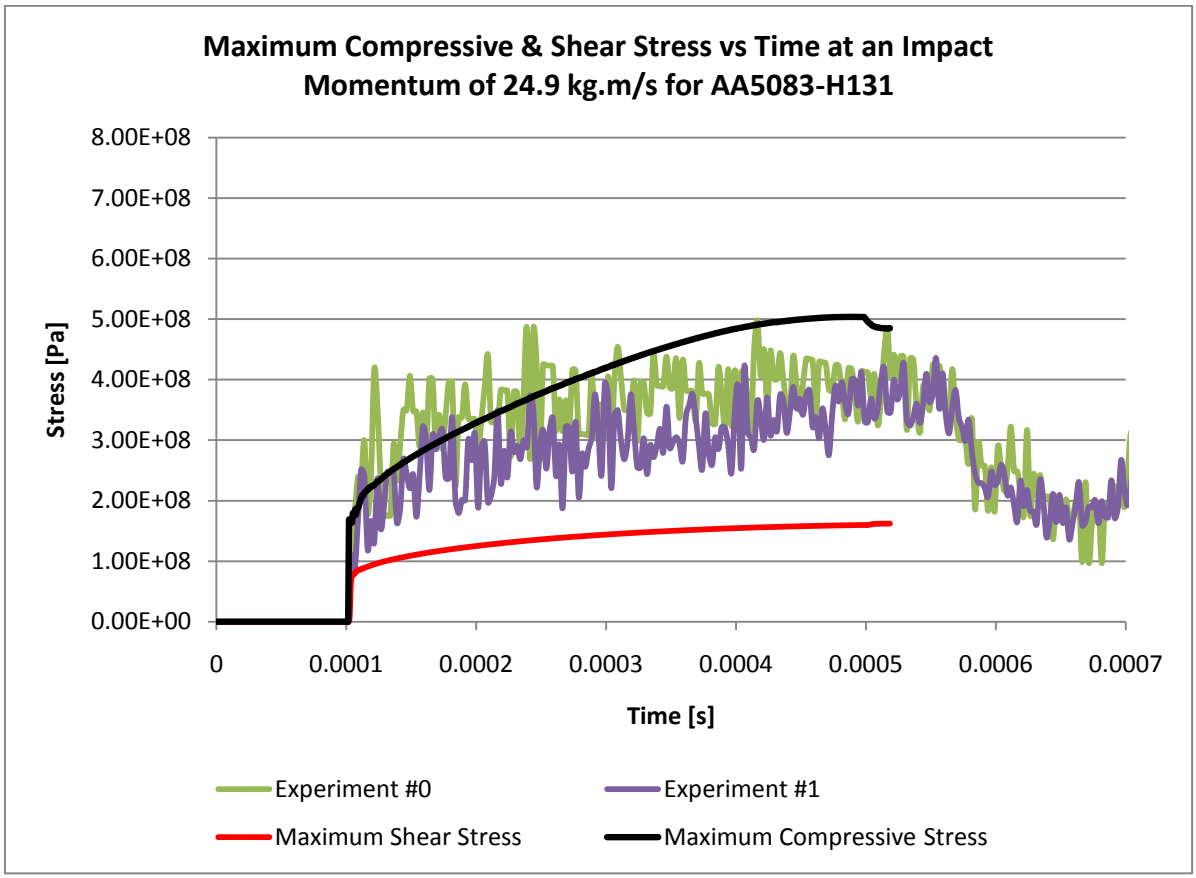

Figure 35. Stress-time history of aluminum alloy 5083-H131 at an impact momentum of 24.9 kg.m/s

(Experimental results from Nazimuddin (2010))

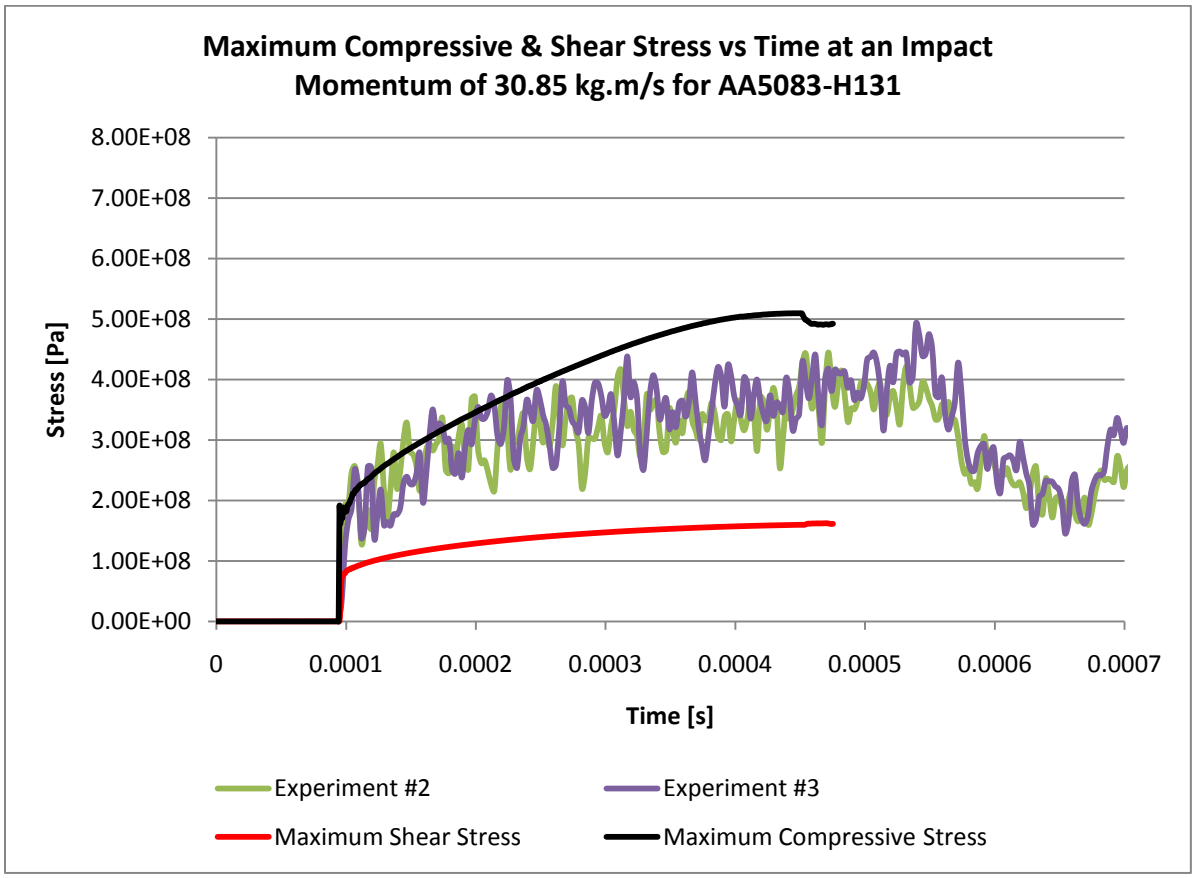

Figure 36. Stress-time history of aluminum alloy 5083-H131 at an impact momentum of 30.85 kg.m/s

(Experimental results from Nazimuddin (2010))

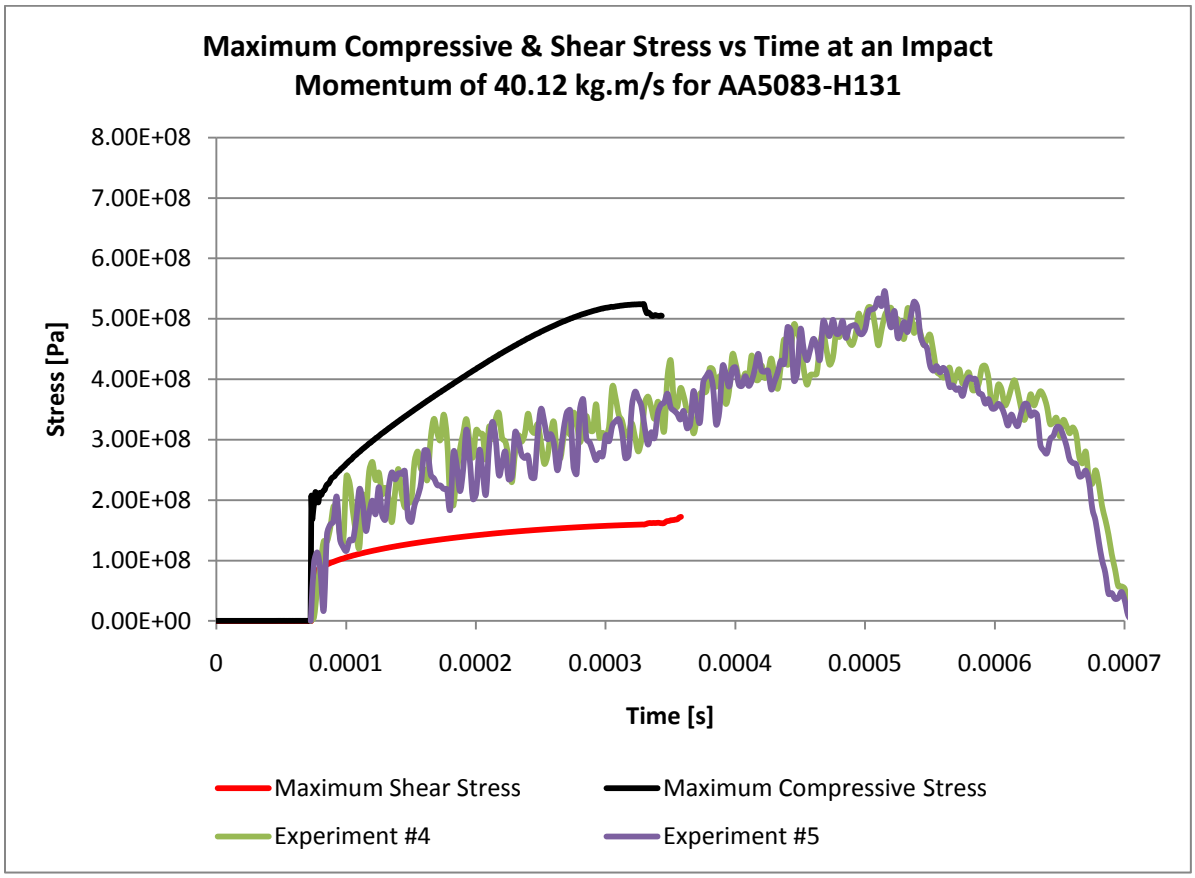

Figure 37. Stress-time history of aluminum alloy 5083-H131 at an impact momentum of 40.12 kg.m/s

(Experimental results from Nazimuddin (2010))

The stress-time responses based, on the Johnson-Cook model, seem to retain their basic shape when the impact momentum is increased, but resemble the behavior of BCC metals under these same loading conditions, that is, strain hardening takes place at a faster rate as impact momentum increases. Thus, the higher the impact momentum, the earlier the maximum compressive stress is reached. However, the behavior of aluminum alloy does not follow this convention. The peak stress is reached at almost the same time regardless of impact momentum.

In their experimentation, Lee and Chen (2006) proved that the flow behavior of aluminum alloys and FCC metals is highly strain rate sensitive, showing that the flow stress of Al-Sc alloy increases by approximately 200 MPa as the deformation strain rate is increased from 10^{-3} s^{-1} to 1200 s^{-1}. They showed that the flow stress increases gradually with increasing strain at a constant strain rate and increases rapidly with increasing strain rate at a constant strain. This supports the assumption that the strain hardening effects of aluminum alloys is dependent on the strain rate.

The Johnson-Cook model has no dependencies between the strain rate and strain hardening effects, as was shown previously. The Johnson-Cook hardening law in an empirical approximation of the quasi-static stress strain curve basing the shape of the strain hardening on quasi-static data at a constant strain rate. In order to properly describe the behavior of FCC metals, the Johnson-Cook model must be modified to include a dynamically changing strain hardening coefficient and sensitivity based on multiple strain rates. This would not only increase the difficulty in obtaining the coefficients but may introduce an error based on the sheer volume of experimental results necessary to

formulate such constants. In cases like these, physical based models may be more appropriate, such as the Feng and Bassim model described previously.

6. CONCLUSIONS

The purpose of this research was to investigate the high strain rate behavior of selected armor materials in compression through finite element modeling based on the Johnson-Cook visco-plastic constitutive equations. This model was selected for its ease of use and dependencies on readily available experimental data. Evaluation of the model was conducted through comparison with experimental data for each of the armor materials supplied by The Canadian Department of National Defence. Dynamic stress-time responses were generated for a range of impact momentums and failure modes were identified linking them to the possibility of adiabatic shear band formation.

The following conclusions can be drawn from the results of the finite element modeling:

- The Johnson-Cook model can be used to model the plastic behavior of BCC metals to a relatively high degree of accuracy, up to the point of thermal instability. While insensitive to minute physical and microstructural changes in the metal, it can depict large fluctuations in the dynamic stress response caused by possible nucleation of transformed shear bands which lead to complete shear failure in the specimen.

- At certain impact momentums, shear failure in the specimen nucleates at the center and then propagates outward towards the edges, in a fashion depicted in Figure 27. This is reflected in several experiments conducted at conditions of high strain rate compression.

- The Johnson-Cook model does not show the effects of thermal softening. Because the model is purely phenomenological, the strain, strain rate, and temperature dependencies of the flow stress are only used to scale the overall behavior of the metal. As a result the deformation, fracture, and failure are driven solely by mechanical instabilities.

- Impact momentums that show complete shear failure in the modeled results are in close agreement with momentums conducive to shear band formation observed in experimental work for both Maraging Steel 300 and High Hardness Armor (HHA).

- Nucleation of shear failure in the center of the specimen causes a drop in the maximum compressive stress in the modeled results. The time at which this maximum compressive stress is reached matches closely with experimental instability results for both BCC armor metals tested.

- The Johnson-Cook model is not quite valid for FCC metals, which are highly strain rate sensitive and exhibit a large plastic region compared to the two BCC armor steels tested. For these metals, strain hardening and temperature effects are dependent on the strain rate while in the Johnson-Cook model, these are considered to be all independent of one another and both strain hardening and strain rate sensitivity are regarded as constant.

REFERENCES

"ABAQUS Users' Manual." 2008.

Al-Ameeri, S. "The Effect of Heat Treatment on the Adiabatic Shear Bands in AISI 4340 Steel at High Strain Rate." Masters Thesis, Department of Mechanical Engineering, The University of Manitoba, Winnipeg, 2005.

Argon, A.S. "The Homogeneity of Plastic Deformation." *A.S.M.*, 1973: 161.

Armstrong, R.W., and F.J Zerilli. "Dislocation mechanics aspects of plastic instability and shear banding." *Mechanics of Materials* 17 (1994): 319-327.

Ashkenazi, Dana. "Fracture-Crack Mechanics in Bimaterial Interface." PhD Thesis, Department of Mechanical Engineering, Tel Aviv University, 2000.

Ashkenazi, Dana. "Investigating material failures: were the titanic and challenger disasters preventable?" *Galileo* 103 (2007).

ASM International. *Atlas of Stress-strain Curves.* Edited by Y. Tamarin. ASM International: The Materials Information Society, 2002.

ATI Properties Inc. "Vascomax Technical Data Sheet." Monroe, NC: Allvac: An Allegheny Technologies Company, 2000.

Backman, M.E., and S.A. Finnegan. "Metallurgical effects at high rates of strain." (Plenum Press) 1973: 531-543.

Backofen, W.A. "Fracture on engineering materials." *A.S.M*, 1964: 107.

Bai, Y. *Shock Waves and High-Strain-Rate Phenomena in Metals.* Edited by M.A. Meyers and L.E. Murr. New York: Plenum Press, 1981. 277-84.

Baron, H.G. *Journal of Iron and Steel Inst.* 182 (1956): 354.

Basinski, Z.S. "Thermally activated glide in face-centered cubic metals and its application to the theory of strain hardening." *Philosophical Magazine* 4 (1959): 393-432.

Bassim, M.N, and N. Panic. "High strain rate effects on the strain of alloys steels." *Journal of Materials Processing Technology* 92-93 (1999): 481-485.

Becker, R, and O Richmond. "Incorporation of microstructure geometry in material modeling." *Model Simulations in Material Science Engineering* 2 (1993): 439-454.

Benck, R.F., and G. Silsby. *Quasistatic Compression & Tensile Stress-Strain Curves, Tantalum-10% Tunsten and 300 Grade Maraging Steel.* Aberdeen Proving Ground, Maryland: US Army Ballistics Research Laboratory, 1986.

Bisalloy Steels Australia Pty Ltd. "Bisplate Technical Guide." Australia: Bisalloy Steels, 2008. 14.

Blicharksi, M., R. Becker, and H. Hu. "Deformation texture of channel-die deformed aluminum bicrystals with S orientations." *Acta Metall. Mater.* 41 (1993): 2007-16.

Brokenbrough, J.R., W.H. Hunt Jr., and O. Richmond. "A reinforced material model using actual microstructural geometry." *Scr. Metall. Mater.* 27 (1992): 385-390.

Buchar, J, J Voldrich, S Role, and J Lisy. "Ballistics Performance of Dual Hardness Armour." *20th International Symposium on Ballistics.* Orlando, FL, 2002.

Burns, T.J., D.E. Grady, and L.S. Costin. "Shock waves in condensed matter." *Amer. Phys. Soc.*, 1982: 372-5.

Callister, William D. Jr. *Fundamentals of Materials Science and Engineering.* Danvers, MA: John Wiley & Sons, 2005.

Campbell, J.D. *Material Science and Engineering.* 1973.

Campbell, J.D., and W.G. Ferguson. "Temperature and strain-rate dependence of the shear strength of mild steel." *Philosophical Magazine* 21 (1970): 63-82.

Canas, J., R. Picon, F. Paris, A. Blazquez, and J.C. Marin. "A simplified numerical analsysis of residual stresses in aluminum welded plate." *Comp. & Structures* (Department of Continuum Mechanics, Industrial Engineering School, University of Seville) 58, no. 1 (June 1994): 59-69.

Cepus, E. "Evolution of Adiabatic Shear Bands in High Strength Steels at High Shear Strain Rates." Department of Mechanical and Manufacturing Engineering, The University of Manitoba, Winnipeg, 1995.

Clifton, R.J., J. Duffy, K.A. Hartley, and T.G. Shawki. "On critical conditions for shear band formation at high strain rates." *Scripta Metallurgica* 18 (1984): 442.

Cubberly, W.H,, and B. Ramon. *Desk Edition: Tool and Manufacturing Engineers' Handbook.* Society of Manufacturing Engineers, 1989.

Culver, R.S. *Proc. 3rd Int. Conf. of the Centre for High Energy Forming.* 1971.

Culver, R.S. "Metallurgical effects at high strain rates." *ed. R.e. al.*, 1973: 519.

Dodd, B., and A.G. Atkins. *Acta Metall.* 31 (1983): 9-15.

EIToby, M.S., E. Ng, and M.A. Elbestawi. "Finite element modeling of erosive wear." *International Journal of Machine Tools & Manufacture* 45 (June 2004): 1337-1346.

Feng, H, and M.N Bassim. "Finite element modeling of the formation of adiabatic shear bands in AISI 4340 steel." *Material Science and Engineering* A266 (1999): 255-260.

Follansbee, P.S., and U.F. Kocks. "A constitutive description of the deformation of copper based on the use of the mechanical threshold stress as an internal state variable." *Acta Metall.* 36 (1988): 81-93.

Frenkel, J. "Zur Theorie der Elastizitatsgrenze und der Festigkeit Kristallinischer Korper." *Z. Phys* 37 (1926): 572-609.

Ghoniem, N.M., and S.H., Sun, L.A. Tong. "Parametric dislocation dynamic: a thermodynamics-based approach to investigations of mesoscopic plastic deformation." *Phys. Rev.* B, no. 61 (2000): 913-927.

Gosh, S., K. Lee, and S. Moorthy. "Two scale analysis of heterogeneous elastic-plastic materials with asymptotic homogenization and voronoi cell finite element model." *Computational Methods in Applied Mechanical Engineering* 132 (1996): 63-116.

Gray III, G.T, S.R. Chen, W. Wright, and M.F. Lopez. *Constitutive Equations for Annealed Metals Under Compression at High Strain Rates and High Temperatures.* Los Alamos, NM: Los Alamos National Laboratory, 1994.

Grebe, H.A., H.R. Pak, and M.A. Meyers. "Adiabatic shear localization in titanium and Ti-6 Pct Al-4 Pct V alloy." *Metallurgical Transactions A* 16A (1985): 761-75.

Grytten, Frode, Egil Fagerholt, Trond Auestad, Bernt Forre, and Tore Borvik. "Out-of-plane deformation measurements of an aluminum plate during quasi-static perforation using structural light and close-range photogrammetry." *International Journal of Solids & Structures*, no. 44 (2007): 5752-5773.

Gupta, Y.M., G.E. Duvall, and G.R Fowles. "Dislocation mechanisms for stress relaxation in shocked LiF." *Journal of Applied Physics* 46 (1975): 532-546.

Hahn, G.T. "Model for yielding with special reference to yield-point phenomena of iron and related BCC metals." *Acta Metallurgica* 10 (1962): 727-738.

Hall, E.O. "The deformation and ageing of mild steel: III discussion of results." *Proc. Roy. Soc.* B, no. 64 (1951): 747-753.

Huang, M., Pedro E.J. Rivera-Diaz-del-Castillo, Olivier Bouaziz, and Sybrand van der Zwaag. "A constitutive model for high strain rate deformation in FCC metals based on irreversible thermodynamics." *Mechanics of Materials* 41 (2009): 982-988.

Hull, D., and D.J. Bacon. *Introduction to Dislocations, Fourth Edition.* Jordan Hill, Oxford: Butterworth-Heinemann, 2001.

Hunt Jr., W.H, O Richmond, and R.D Young. "Fracture initiation in particle hardened materials with high volume fraction." *Proceedings of the 6th International Conference on Composite Materials* 2 (1987): 2.209.

Johnson, J.R., and W.H. Cook. "Fracture characteristics of three metals subjected to various strains, strain rates, temperatures and pressures." *Engineering Fracture Mechanics* 21 (1985): 31-48.

Kalish, David, and H.J. Rack. *Thermal Embrittlement of 18Ni(350) Maraging Steel.* Report, Marietta, GA: The Metallurgical Society of AIME, 1971.

Kapoor, Rajeev, and Sia Nemat-Nasser. "Comparison between high and low strain-rate deformation of tantalum." *Metallurgical and Materials Transactions A* 31A (2000): 815-823.

Kennan, Z. *Determination of the Constitutive Equations for 1080 Steel and Vascomax 300.* Masters Thesis, Department of the Air Force Air University, Ohio: Wright-Patterson Airo Force Base, 2005.

Klepaczko, J.R. "Plastic shearing at high and very high strain rates." *Journal de Physique IV* 4 (1994): 35-40.

Kocks, U.F., A.S. Argon, and M.F. Ashby. *Progr. Mater. Sci.* 19 (1975): 1-271.

Kuriyama, S., and M.A. Meyers. "Numerical Analaysis of Adiabatic Shear Band in an Early Stage of its Propagation." *IUTAM Symposium.* 1987. 203.

Lee, Woei Shyan, and Tao Hsing Chen. "Rate-dependent deformation and dislocation substructure of Al-Sc alloy." *Scripta Materiala* 54 (2006): 1463-1468.

Lee, Woei Shyan, Chi Feng Lin, Tao Hsing Chen, and Hsin Hwa Hwang. "Correlation of dynamic impact properties with adiabatic shear banding behaviour in Ti-15Mo-5Zr-3Al alloy." *Materials Science and Engineering A* 475 (2008): 172-184.

Lindholm, U.S, and G.R. Johnson. *Material Behavior Under High Stress and Ultra-High Loading Rates.* Edited by J. Mescall and V. Weiss. Plenum Press, 1983. 61-79.

Lindholm, U.S. "Techniques in Metals Research." *Interscience* 1 (1971).

Magnusen, P.E, E.M Dubensky, and D.A Koss. "The effect of void arrays on void linking during ductile fracture." *Acta Metall* 36 (1988): 1503-9.

Magnusen, P.E. *An Analysis of the Ductile Fracture of Void Containing Material: Experimental Modeling and Computer Simulation.* PhD Dissertation, Michigan Technological Universtiy, 1987.

Mirfakhraei, Sahar. "Deformation of High Strength Alloys at High Strain Rates." Masters Thesis, Department of Mechanical and Manufacturing Engineering, The University of Manitoba, Winnipeg, 2008.

Nakkalil, R., J.R. Hornaday Jr., and M.N. Bassim. "Characterization of the compression properties of rail steels at high temperatures and strain rates." *Materials Science and Engineering* A, no. 141 (1991): 247-260.

Nazimuddin, Ghaznafar M. "High Strain Rate Studies of Armor Materials." Masters Thesis, Mechanical Engineering, University of Manitoba, Winnipeg, 2010.

Nemat-Nasser, S., and J. Isaacs. "Direct Measurement of Isothermal Flow Stress of Metals at Elevated Temperatures and High Strain Rates with Applications to Ta and Ta-W Alloys." *Acta Metall* 45 (1997): 907-919.

Nemat-Nasser, S., and W.G. Guo. "Thermomechanical response of HSLA-65 steel plates: experiments and modeling." *Mechanics of Materials* 37 (2005): 379-405.

Nemat-Nasser, S., and Y Li. "Flow stress of FCC polycrystals with application to ORHC Copper." *Acta Mater* 46 (1998): 565-577.

Odeshi, A.G., M.N, Bassim, S. Al-Ameeri, and Q. Li. "Dynamic shear band propagation and failure in AISI 4340 steel." *Journal of Materials Processing Technology* 169 (2005): 150-155.

Odeshi, A.G., M.N. Bassim, and S. Al-Ameeri. "Effect of heat treatment on adiabatic shear bands in a high-strength low alloy steel." *Materials Science and Engineering A* 419 (2006): 69-75.

Olson, G.B., J.F. Mescal, and M. Azrin. *Shock waves and High Straiin Rate Phenomena in Metals.* Edited by M.A. Meyers and L.E. Murr. New York: Plenum Press, 1981. 221-47.

Orowan, E. "Problems of plastic gliding." *Proceedings of the Physical Society* 52 (1940): 8-22.

Panic, Nebojsa. "High Strain Rate Induced Failure in Steels at High Shear Strains." Masters Thesis, Department of Mechanical Engineering, The University of Manitoba, Winnipeg, 1999.

Petch, N.J. "Cleavage strength of polycrystals." *J. Iron Steel Inst.* 174 (1953): 25-28.

Poliak, E.I., and J.J. Jonas. "A one-parameter approach to determining the critical conditions for the initiation of dynamic recrystallization." *Acta Mater.* 44 (1996): 127-136.

Recht, R.F. *Catastrophic Thermoplastic Shear.* ASME, 1964, 189.

Rusinek, A., J.A. Rodriguez-Martinez, and A. Arias. "A Thermo-viscoplastic constitutive model for FCC Metals with application to OFHC copper." *International Journal of Mechanical Sciences*, 2009.

Smelser, R.E., and R. Becker. "ABAQUS user subroutines for material modelling." *Proceedings of the ABAQUS Users' Conference* (Providence, RI: Hibbitt, Karlsson & Sorensen), 1989: 457-72.

Smit, R.J.M, W.A.M Brekelmans, and H.E.H Meijer. "Prediction of the mechanical behavior of nonlinear heterogeneous systems by multi-level finite element modeling." *Computational Methods in Applied Mechanical Engineering* 155 (1998): 181-192.

Staker, M.R. "The relation between adiabatic shear instability strain and material properties." *Acta. Met.* 29 (1981): 683.

Tang, Meijie. "Dislocation Dynamics for Single Crystal Plasticity of BCC Metals." *Physical and Life Sciences Directorate.* March 5, 2009. https://www-pls.llnl.gov/?url=about_pls-condensed_matter_and_materials_division-eos_materials_theory-projects-dd_bcc.

Taylor, Sir G., and A.C. Whiffin. "The use of flat-ended projectiles for determining dynamic yield stress; I theoretical considerations; II tests on various metallic

materials." *Royal Society Proceedings* 194, no. Series A (1948): 289-299 and 300-322.

The Aluminum Association Inc. 2009. http://www.aluminum.org/ (accessed December 2009).

The American Society of Mechanical Engineers. "Split-Hopkinson Pressure Bar Apparatus: A Historic Mechanical Engineering Landmark." *Designation Ceremony, Southwest Research Institute.* Texas: ASME, 2006.

The United States Department of Defense. "Army Materials Research: Transforming Land Combat Through New Technologies." *AMPTIAC Quarterly* (Department of Defense Information Analysis Center) 8, no. 4 (2004).

Thomson, Alan C. "High Strain Rate Characterization of Advanced High Strength Steels." Masters Thesis, Department of Mechanical Engineering, University of Waterloo, Waterloo, 2006.

United States of America Department of Defense. "Military Handbook: Metallic Materials and Elements for Aerospace Vehicle Structures." *Granta Design.* December 1, 1998. http://www.grantadesign.com/userarea/Mil/mil5.htm (accessed 2009).

Vinh, T., M. Afzali, and A. Roche. *3rd Int. Conf. Mech. Behav. Mat. (ICM3).* Vol. 2. Edited by K.J. Miller and R.F. Smith. Cambridge, 1979. 633-43.

Wessel, James K. *Handbook of Advanced Materials: Enabling New Designs.* Oak Ridge, Tennessee: John Wiley & Sons, Inc, 2004.

Xue, Q., D. Benson, M.A. Meyers, V.F. Nesterenko, and E.A. Olevsky. "Constitutive response of welded HSLA 100 steel." *Materials Science and Engineering* A354 (2003): 166-179.

Yazdani, F., M.N. Bassim, and A.G. Odeshi. "The formation of adiabatic shear bands in copper during torsion at high strain rates." *Mesomechanics*, 2009.

Zener, C., and J.H. Hollomon. "Effect of strain rate upon plastic flow of steel." *Journal of Applied Physics* 15 (1944): 22.

Zerilli, F.J, and R.W Armstrong. "Dislocation-mechanics-based constitutive relations for material dynamics calculations." *Journal of Applied Physics* 61 (1987): 1816-1825.

Zurek, A.K., P.S. Follansbee, and D. Kapoor. "High strain rate behavior of refractory metals and alloys." *TMS*, 1992: 190-207.